

1 **JWST Coronagraphic Images of 14 Her c:**
2 **a Cold Giant Planet in a Dynamically Hot, Multi-planet System**

3 **DANIELLA C. BARDALEZ GAGLIUFFI**^{1,2,*} **WILLIAM O. BALMER**^{3,4,*} **LAURENT PUEYO**⁴ **TIMOTHY D. BRANDT**⁴
4 **MARK R. GIOVINAZZI**¹ **SARAH MILLHOLLAND**^{5,6} **BRENNEN BLACK**⁵ **TIGER LU**⁷ **MALENA RICE**⁷ **JAMES MANG**⁸
5 **CAROLINE MORLEY**⁸ **BRIANNA LACY**^{9,10} **JULIEN GIRARD**⁴ **ELISABETH MATTHEWS**¹¹ **AARYNN CARTER**⁴
6 **BRENDAN P. BOWLER**¹² **JACQUELINE K. FAHERTY**² **CLEMENCE FONTANIVE**¹³ **AND EMILY RICKMAN**¹⁴

7 ¹*Amherst College, Department of Physics and Astronomy, Department of Physics & Astronomy, Amherst College, 25 East Drive,*
8 *Amherst, MA 01002, USA*

9 ²*American Museum of Natural History, Department of Astrophysics, 200 Central Park West, New York, NY 10024, USA*

10 ³*Department of Physics & Astronomy, Johns Hopkins University, 3400 N. Charles Street, Baltimore, MD 21218, USA*

11 ⁴*Space Telescope Science Institute, 3700 San Martin Drive, Baltimore, MD 21218, USA*

12 ⁵*Department of Physics, Massachusetts Institute of Technology, Cambridge, MA 02139, USA*

13 ⁶*Kavli Institute for Astrophysics and Space Research, Massachusetts Institute of Technology, Cambridge, MA 02139, USA*

14 ⁷*Department of Astronomy, Yale University, New Haven, CT 06511, USA*

15 ⁸*Department of Astronomy, University of Texas at Austin, Austin, TX 78712, USA*

16 ⁹*Department of Astronomy, University of California, Santa Cruz, CA 95064, USA*

17 ¹⁰*Bay Area Environmental Research Institute + NASA Ames Research Center, Moffett Field, CA 94035, USA*

18 ¹¹*Max-Planck-Institut für Astronomie, D-69117 Heidelberg, Germany*

19 ¹²*Department of Physics, University of California, Santa Barbara, CA 93106, USA*

20 ¹³*Institute for Research on Exoplanets, University of Montréal, Montréal, QC H3A 2A7, Canada*

21 ¹⁴*European Space Agency (ESA), ESA Office, Space Telescope Science Institute, 3700 San Martin Drive, Baltimore MD, 21218*

22 Submitted to The Astrophysical Journal Letters

23 **ABSTRACT**

24 Most observed multi-planet systems are coplanar, in a dynamically “cold” configuration of concentric
25 orbits like our own Solar System. With the James Webb Space Telescope (JWST) we have detected
26 14 Her c, the first mature and cold exoplanet directly imaged in a dynamically “hot”, multi-planet
27 system. With large eccentricities and a nonzero mutual inclination, the present-day architecture of this
28 system points to a turbulent past and ongoing angular momentum exchange between the planetary
29 orbits of 14 Her b and c. The temperature of 14 Her c rivals both the coldest imaged exoplanet and
30 the coldest known brown dwarf. Moreover, its photometry at 4.4 μm is consistent with the presence of
31 carbon disequilibrium chemistry and water ice clouds in its atmosphere. 14 Her c presents a unique
32 laboratory to study giant planet formation, dynamical evolution of multi-planet system architectures,
and atmospheric composition and dynamics in extremely cold worlds.

33 *Keywords:* James Webb Space Telescope (2291), Exoplanets (498), Extrasolar gaseous giant planets
34 (509), Direct imaging (387), Exoplanet atmospheres (487), Exoplanet dynamics (490)

35 **1. INTRODUCTION**

36 The early evolution of our own Solar System was dominated by the dynamical influence of the gas giants (S. N.
37 Raymond 2024). After the dispersal of gas in the protoplanetary disk, Jupiter may have scattered the outer giant
38 planets onto wider orbits, and even possibly prompted the ejection of a fifth giant planet (D. Nesvorný 2011). The
39 final outcome of the migration of the giant planets was our stable Solar System, with Jupiter redirecting ice-rich small

Corresponding author: Daniella C. Bardalez Gagliuffi & William O. Balmer
Email: dbardalezgagliuffi@amherst.edu, wbalmer1@jhu.edu

* These authors contributed equally to this work

bodies inwards as one potential pathway to deliver water to the terrestrial planets and to allow life to thrive on Earth (K. E. Mandt et al. 2024). The putative ejected giant planet fared the opposite fate, and was consigned to wander the Solar neighborhood without a host star as a “rogue planet.” Whether similar histories of dynamical interaction, planet scattering, and ejection are common across planetary systems remains an open question due to the difficulty of precisely mapping exoplanet system architectures and constraining the occurrence rate of isolated rogue planets (T. Sumi et al. 2023). In this paper, we describe the orbital architecture of a nearby exoplanetary system whose dynamically rich history has produced an architecture radically different from our Solar System’s, with two giant planets on misaligned, eccentric orbits, potentially as a result of a planetary ejection. The study of such an extreme planetary system is enabled by our JWST (J. Rigby et al. 2023) detection of the potentially coldest and oldest planet yet imaged.

14 Herculis is a nearby ($d = 17.898 \pm 0.009$ pc; Gaia Collaboration et al. 2021), metal-rich ($[\text{Fe}/\text{H}] = 0.43 \pm 0.07$; C. Soubiran et al. 2010), K0-type, solar mass star hosting two giant planets (D. C. Bardalez Gagliuffi et al. 2021). These two massive planets cause a reflex motion on the star detectable as a periodic change in its radial velocity and proper motion. Radial velocity monitoring spanning over 20 years revealed a recurrent 5-year period due to the inner planet, 14 Her b, and a long-term trend (R. A. Wittenmyer et al. 2007) later confirmed as the widely-separated exoplanet 14 Her c by incorporating absolute astrometry from the Hipparcos and Gaia missions (D. C. Bardalez Gagliuffi et al. 2021). This analysis showed that the two planets in the system are roughly located at the equivalent semi-major axes of the asteroid belt and Neptune’s orbits in our own Solar System ($a_b = 2.845^{+0.039}_{-0.03}$ au, $a_c = 27.4^{+7.9}_{-16}$ au), yet on very eccentric ($e_b = 0.369 \pm 0.003$, $e_c = 0.64 \pm 0.13$), extremely misaligned orbits ($\Theta_{bc} = 96.3^{+36.8}_{-29.1}$ °). Only a handful of other multi-planet systems have a measured orbital misalignment between two of their planetary orbits (e.g., π Men, R. J. De Rosa et al. 2020; J. W. Xuan & M. C. Wyatt 2020; ν And, B. E. McArthur et al. 2010; R. Deitrick et al. 2015; Kepler-108, S. M. Mills & D. C. Fabrycky 2017; HAT-P-11, J. W. Xuan & M. C. Wyatt 2020; Q. An et al. 2025; T. Lu et al. 2025; HD 73344, J. Zhang et al. 2024; HD 3167, V. Bourrier et al. 2021), yet none of these planets have been directly imaged. While direct imaging is a challenging technique due to the large contrast between star and planet, it can provide firsthand information on the planet, its exact location, and its atmosphere.

The measured dynamical masses of the 14 Her planets ($M_b = 9.1 \pm 1.9 M_J$, $M_c = 6.9^{+1.6}_{-1.0} M_J$) at the age of the system ($4.6^{+3.8}_{-1.3}$ Gyr) imply they have extremely cold temperatures (250 – 300 K; D. C. Bardalez Gagliuffi et al. 2021), making them far more comparable to our own Jupiter (125 K; R. Hanel et al. 1981) than the majority of directly imaged exoplanets (700-1700 K; B. P. Bowler 2016), except for ϵ Indi Bb (E. C. Matthews et al. 2024a), and TWA-7b (A. M. Lagrange et al. 2025a). Cold exoplanets (< 500 K) emit most of their light in the mid-infrared, and are therefore difficult to image from the ground in the optical or near-infrared, because of their intrinsic faintness and large flux ratio, or ‘contrast,’ with their host stars. With its space-based, mid-infrared capabilities, JWST has the unique ability to directly image much colder planets than have been studied before.

In this paper we present the first direct image of the nearby, cold, mature, giant planet 14 Her c with JWST/NIRCam coronagraphy and revise its orbital parameters. This is the first direct image of a planet in a significantly misaligned planetary system. In Section 2 we describe the new direct imaging observations with JWST/NIRCam and the process to measure the photometry and astrometry of 14 Her c. In Section 3 we describe the updated orbit fitting, evolutionary and atmospheric modeling, and dynamical simulations of the orbits. In Section 4, we discuss our results and their implications for the mutual inclination of the planetary orbits, the likelihood of disequilibrium chemistry in the planet’s atmosphere, and the time evolution of the planetary orbits. We present our conclusions in Section 5. Technical details about our methods on image reduction, orbit fitting, evolutionary and atmospheric modeling, and N-body simulations are summarized in the Appendix (Sections A-C).

2. OBSERVATIONS AND DATA REDUCTION

We used JWST/NIRCam (M. J. Rieke et al. 2023) to image 14 Her c as the main science objective of Cycle 2 program GO 3337 (PI: Bardalez Gagliuffi, Co-PI: Balmer). Our observing strategy relied on both Angular Differential Imaging (ADI) and Reference Differential Imaging (RDI) to perform starlight subtraction (K. B. Follette 2023, for a recent review). For validation, we used the `pyNRC`¹ (J. Leisenring et al. 2022) and `PanCAKE`² Python packages to determine optimal instrument readout patterns and estimate the contrast performance of the observations. Our

¹ <https://pynrc.readthedocs.io/en/latest/>

² <https://aarynncarter.github.io/PanCAKE>

89 NIRCam observations of 14 Her c were carried out between May 18, 2024 18:31:45 and May 19, 2024 01:08:45 (UTC) for
 90 a total of 7.8 hours (including observatory overheads) simultaneously with the F200W and F444W filters and using the
 91 MASKA335R coronagraph (J. E. Krist et al. 2010) at position angles 191.87° and 181.87° . This science observation
 92 used the SHALLOW4 readout pattern at 10 groups per integration and 96 integrations per exposure. Immediately
 93 following the observation of the target, we observed the reference star HD 144002 using the SHALLOW4 readout pattern,
 94 8 groups per integration, and 16 integrations per exposure, with the 9-POINT-CIRCLE small grid dither pattern in an
 95 uninterrupted sequence to preserve the similarity of the telescope wavefront between observations. Observing the
 96 reference star with the small grid dither increases the diversity of the reference Point Spread Function (PSF) library
 97 (R. Soummer et al. 2014). We selected this reference star based on its relative on-sky proximity to 14 Her ($\rho=3.67^\circ$ in
 98 J2016), its brighter K -band magnitude, yet similar spectral type, and its low *Gaia* Renormalised Unit Weight Error
 99 (RUWE = 0.986, L. Lindegren 2018), which indicates that it is likely a single star.

100 The observations were designed to detect a 250 K source at $1''.3$ from the star at a contrast of 10^{-6} with a 5σ
 101 confidence in the F444W filter, while simultaneously collecting parallel images in the F200W filter where the planet
 102 signal was not expected. The limit in F200W-F444W color allows for the rejection of the vast majority of potential
 103 background contaminants, including stars, galaxies, and quasars, which would be at least as bright in F200W in
 104 comparison to F444W. The MASKA335R mask was chosen to balance inner working angle (IWA), raw starlight
 105 suppression performance, and reliable target acquisition.

106 Image reduction and calibration followed previous work on the JWST/NIRCam coronagraph (A. L. Carter et al.
 107 2023; K. Franson et al. 2024a; W. O. Balmer et al. 2025), the details of which are recorded in Appendix A³. The
 108 residual starlight in the coronagraphic images was modeled and removed using the Karhunen–Loève Image Projection
 109 (KLIP) algorithm (R. Soummer et al. 2012) through the Python implementation pyKLIP⁴ (J. J. Wang et al. 2015)
 110 wrapped by spaceKLIP⁵.

111 The JWST image of 14 Her c is shown in Figure 1. We detected a point source in the F444W filter with a signal-to-
 112 noise ratio of 5.7σ , an angular separation of $1''.115 \pm 0''.005$ at a position angle of $225.84^\circ \pm 0.26^\circ$ East of North, and
 113 apparent magnitude of 19.68 ± 0.07 mag with reference to Vega. There is also a spatially resolved background galaxy
 114 $1''.5$ away and to the SE of the star in both F200W and F444W images, whereas the point source only appears in the
 115 F444W image as expected for a cold giant planet. The location of our point source is consistent within 1σ with the
 116 latest predictions of the location of 14 Her c based on orbital solutions from the literature (G. F. Benedict et al. 2023,
 117 reproduced from their Table 10).

118 2.1. Contrast curves

119 We estimated the contrast performance of our observations using the spaceKLIP package following previous work (J.
 120 Kammerer et al. 2022; A. L. Carter et al. 2023). We measured the annular standard deviation of the starlight-subtracted
 121 images, masking the positions of the two sources within $2''.0$ (the planetary point source and the bright extended galaxy).
 122 The raw contrast was corrected for small number statistics in the innermost annuli using the Student t-distribution
 123 correction following D. Mawet et al. (2014). The corrected contrast was then calibrated into physical units using a
 124 synthetic BT-NextGen model stellar spectrum (F. Allard et al. 2011) with parameters $T_{\text{eff}}=5300$ K, $\log(g)=4.5$, and
 125 $[\text{Fe}/\text{H}]=+0.5$ (G. Gonzalez et al. 1999; D. C. Bardalez Gagliuffi et al. 2021), scaled to match the Hipparcos/Tycho2 (E.
 126 Høg et al. 2000), *Gaia* (Gaia Collaboration et al. 2022), and 2MASS (M. F. Skrutskie et al. 2006) photometry reported
 127 for 14 Her. The coronagraph transmission function⁶ was applied to the calibrated contrast. Finally, we determined
 128 the starlight subtraction throughput via injection-recovery tests⁷. Figure 6 shows our final calibrated contrast curves.
 129 The observations are sensitive to sources with contrast $\sim 4 \times 10^{-7}$ at $1''.0$ in the F444W filter, and $\sim 3 \times 10^{-7}$ at $1''.0$ in
 130 the F200W filter at 5σ confidence, slightly exceeding our anticipated contrast performance of 10^{-6} at $1''.0$.

131 2.2. Photometry and astrometry of 14 Her c

132 The process of the starlight subtraction with ADI and RDI oversubtracts astrophysical sources present in the
 133 image. We forward-modeled this degradation of the PSF (L. Pueyo 2016) in order to obtain accurate and unbiased
 134 astrometry and photometry of 14 Her c using pyklip (J. J. Wang et al. 2015; J. Golomb et al. 2021) and spaceKLIP

³ A notebook that can be used to reproduce the data reduction and image analysis described in Appendix A can be found online at the
 DOI: <https://doi.org/10.5281/zenodo.15483953> (W. O. Balmer 2025)

⁴ <https://pyklip.readthedocs.io/en/latest/>

⁵ <https://spaceklip.readthedocs.io/en/latest/>

⁶ The NIRCam MASKA335R coronagraph transmission is an axisymmetric function of separation from the center of the mask, see Figure 4
 in J. E. Krist et al. (2010).

⁷ We refer the reader to §3.1 and §3.2 in A. L. Carter et al. (2023) for additional details.

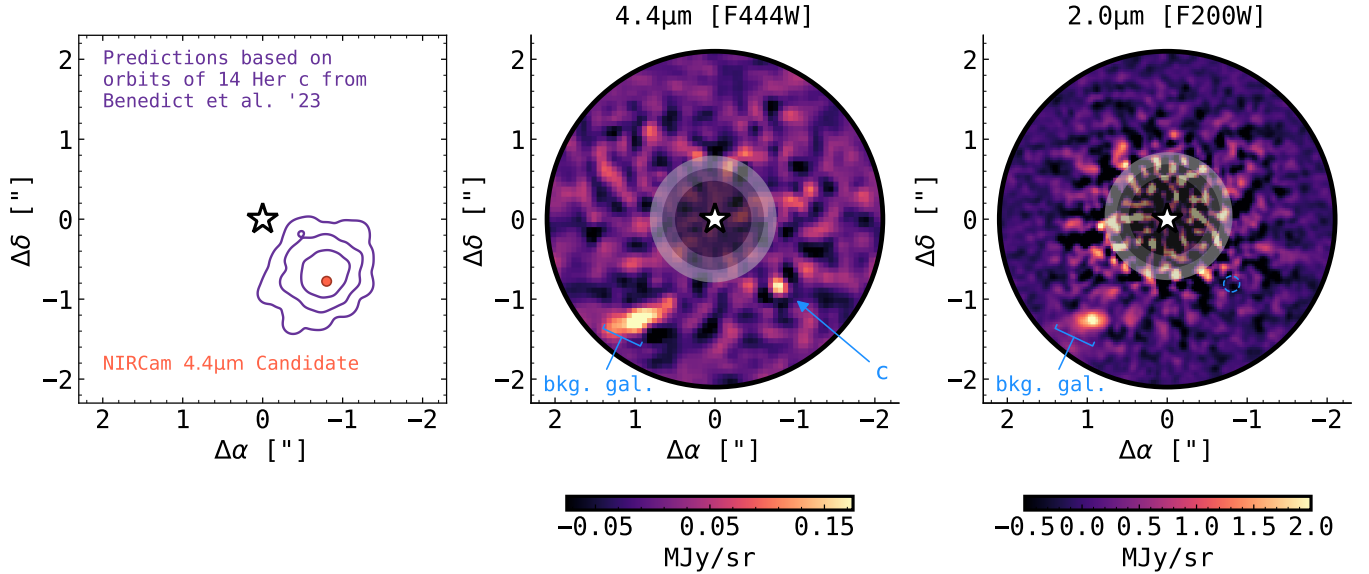


Figure 1. First direct image of 14 Her c. JWST/NIRCam coronagraphic imaging of the 14 Her system with the MASKA335R coronagraph (transmission indicated by gray shaded circles). North is up, east is left. *Left:* Prediction for the location of 14 Her c from a reproduction of the orbits presented in (G. F. Benedict et al. 2023), at the epoch of observation (MJD=60449), and the location of the point source detected in the F444W filter. *Middle:* A starlight-subtracted image taken with the F200W filter (1.755–2.227 μm), showing extended emission from a background galaxy at about 1".5 to the SE from the host star. No other statistically significant point sources are apparent, as intended, given the cold temperature of the planet 14 Her c. *Right:* A starlight-subtracted image taken with the F444W filter (3.881–4.982 μm), showing extended emission from the same background galaxy, and a point source at 1".1 to the SW with a contrast of 1×10^{-6} . The location of the point source, detected with a contrast of 9.6×10^{-7} , agrees within 1σ with the predicted location for the planet, so we conclude we have detected 14 Her c.

(J. Kammerer et al. 2022; A. L. Carter et al. 2023; J. Kammerer et al. 2024; K. Franson et al. 2024b). Briefly, an off-axis coronagraphic PSF model was generated using `webbpsf` at the approximate position of the candidate. The model was scaled, translated, and subtracted from the data to compute a likelihood function, while the scale and translation parameters were sampled iteratively using the `MultiNest` (via `pyMultiNest`) sampling algorithm (F. Feroz et al. 2009; J. Buchner et al. 2014) with 400 live points. We accounted for the presence of correlated noise in the image by sampling the length-scale of a Gaussian process, parameterized using a Matérn $\nu = 3/2$ kernel, which approximates residual speckle noise (J. J. Wang et al. 2016). Once the astrometry and photometry were measured in detector units, they were transformed into physical units accounting for the coronagraphic transmission, filter zero-points, and system distance (A. L. Carter et al. 2023; K. Franson et al. 2024b), with systematic uncertainties on the star-behind-mask position (0.05 pix) and stellar magnitude (0.02 mag) added in quadrature (J. H. Girard et al. 2024). The point source has a relative RA, Dec. $-0''.800 \pm 0''.004$, $-0''.777 \pm 0.006$ (i.e., separation $\alpha = 1''.115 \pm 0''.005$ and position angle $\text{PA} = 225.84 \pm 0.26^\circ$, with a correlation $\rho = -0.5$). We derived an apparent magnitude of 19.68 ± 0.07 mag in the F444W filter, and an upper limit of 19.0 mag in the F200W filter. The corresponding fluxes in SI units are $f_{\text{F444W}} = 3.92 \times 10^{-19} \pm 2.5 \times 10^{-20} \text{ W/m}^2/\mu\text{m}$ and $f_{\text{F200W}} = 7.25 \times 10^{-19} \text{ W/m}^2/\mu\text{m}$, respectively. These fluxes correspond to absolute magnitudes of $M_{\text{F444W}} = 18.42 \pm 0.07$ mag and $M_{\text{F200W}} \geq 17.74$ mag. The candidate point source was recovered in the F444W filter at a signal-to-noise ratio of $\text{SNR} = 5.7\sigma$, or a Bayesian evidence ratio of $\ln(B_{10}) = \ln(Z_1/Z_0) = 115$ by comparing companion contrast to the annular contrast.

2.3. Planetary Prior Probability Compared Against Interloper Probability

JWST is sensitive to background extragalactic sources far fainter than exoplanets in the Solar neighborhood. Previous high contrast imaging campaigns have ruled out sources surrounding 14 Her down to $15 - 30 M_J$ at 1".0 (K. L. Luhman & R. Jayawardhana 2002; J. Patience et al. 2002; J. C. Carson et al. 2009; T. J. Rodigas et al. 2011; S. Durkan et al. 2016). The red F200W-F444W color lower limit of the point source can be used to reject the vast majority of galactic contaminants. Since the probability of late T- or early Y-dwarf contaminants in such a compact field of view

158 is vanishingly small (J. D. Kirkpatrick et al. 2024; E. Bogat et al. 2025), we conclude that the dominant source of
 159 contamination in our images is extragalactic sources.

160 In order to empirically estimate the number of contaminating sources that could confound a detection of 14 Her c,
 161 we calculated a space density of galaxies at all redshifts from JWST images that have similar observed characteristics
 162 as the planet. Following E. Bogat et al. (2025), we acquired the JADES GOODS-S Deep High Level Science Product
 163 v2 from MAST⁸ (D. J. Eisenstein et al. 2023; M. J. Rieke et al. 2023) covering 25 square arcminutes.

164 We define a contaminant as a JADES source that appears point-like in the F444W filter, with a magnitude within the
 165 range of uncertainties of our candidate point source photometry, and with the F200W - F444W color lower limit of our
 166 point source. Specifically, we selected galaxies with AB magnitudes and colors comprised between $[F444W_{\text{AB mag}}] =$
 167 22.9 ± 1.4 mag, and $[F200W_{\text{AB mag}} - F444W_{\text{AB mag}}] = 1.3$, and with a circular-equivalent size of $\text{FWHM} < 4$ pix. We
 168 scaled the resulting number of sources by the sky area covered by the JADES GOODS-S Deep field to calculate the
 169 space density of galaxies with these characteristics. As our candidate source has an F444W magnitude well within
 170 the completeness limits of extragalactic surveys with JWST⁹, and since the completeness corrected source counts
 171 for extragalactic surveys with JWST appear to agree well (E. Merlin et al. 2024, their Figure 7), we do not expect
 172 any slight variation between JADES and other JWST deep fields to affect the robustness of the contaminant fraction
 173 estimate presented here.

174 For the predicted location of 14 Her c (G. F. Benedict et al. 2023) and its 1, 2, and 3 σ contours (see leftmost panel
 175 of Figure 1), we expect on average 0.003, 0.013, or 0.052 contaminating galaxies, respectively. Within 2''0 of 14 Her
 176 A (see center and rightmost panel of Figure 1), we expect on average 0.2 contaminating galaxies. Therefore, given
 177 the small area where the planet is expected, the existence of an extragalactic source with photometric properties that
 178 mimic those of the planet is extremely unlikely. A larger number of extended and blue JADES sources are expected
 179 within 2''0, as evidenced by our detection of a resolved, blue galaxy to the SE of 14 Her A.

180 Balancing the extremely low likelihood that the point source is an extragalactic contaminant, and given that it is
 181 found in the predicted location, and with the expected luminosity for a giant planet of the age of the system (~ 18 mag,
 182 see §3.2), based on evolutionary models (M. S. Marley et al. 2021a), we conclude that the observed point source to
 183 the SW of the star is indeed 14 Her c.

184 This background contaminant analysis emphasizes the importance of prior information, especially system-specific
 185 dynamical priors, when attempting to confirm the existence of directly imaged companions in the infrared with a
 186 facility as sensitive as JWST (E. Bogat et al. 2025). The strong prior prediction for the location of the planet allows
 187 us to robustly claim a reliable detection despite the 0.2 probability of finding a “14 Her c”-like source within the inner
 188 2''0 of our image, and without requiring a follow-up observation to confirm orbital and/or common proper motion of
 189 the point source.

190 Limits at longer wavelengths (with MIRI or ALMA) are invaluable for reducing the probability a candidate point
 191 source is a background contaminant. For single epoch observations, including both NIRCam and MIRI coronagraphic
 192 imaging appears to be the best practice (and, for nearby stars, may result in sensitivity to colder planets, see R.
 193 Bowens-Rubin et al. 2025). For example, In A. M. Lagrange et al. (2025b), the flux limit of a contaminating galaxy
 194 in the filter of interest (11.4 μm) was 50% across their $\sim 10''$ wide field of view. Only with deep upper limits from
 195 archival SPHERE (and especially) ALMA observations, were they able to reduce the contaminant probability in the
 196 1''5 immediately surrounding TWA 7 to 0.35%. Similarly, a second epoch was required for the eventual confirmation of
 197 ϵ Indi A b (E. C. Matthews et al. 2024b), where a low-significance early recovery of the candidate source in ground-
 198 based data was used to confirm the candidate’s planetary nature. Strong dynamical priors, like those used to confirm
 199 TWA 7 b (A. M. Lagrange et al. 2025b) or 14 Her c, still contain a small probability of yielding false positives, but
 200 they allow for greater confidence in the initial characterization of expected planets. Future long wavelength imaging
 201 of 14 Her c with JWST would provide crucial color and temperature characterization, as well as incontrovertible
 202 confirmation of the planet’s detection.

203 The spatial scales where JWST reaches its deepest contrasts are necessarily those where the risk of background
 204 contamination becomes large. Future studies, especially large coronagraphic surveys of young moving group stars with
 205 NIRCam dual-band coronagraphy (GO 4050, 5835, 6005, 7651) will need to rely heavily on ground-based upper limits

⁸ <https://doi.org/10.17909/8tdj-8n28>

⁹ JADES, and other JWST surveys, are 100% complete to at least $[F444W_{\text{AB mag}}] = 28$ mag, whereas our point source has $[F444W_{\text{AB mag}}] = 22.9 \pm 1.4$ mag. See Figure 4 of E. Merlin et al. (2024) for more details.

206 from the literature, as well as any and all available dynamical limits to confirm cold planets that can currently only
 207 be detected with JWST.

208 3. ANALYSIS AND RESULTS

209 3.1. Orbit fitting

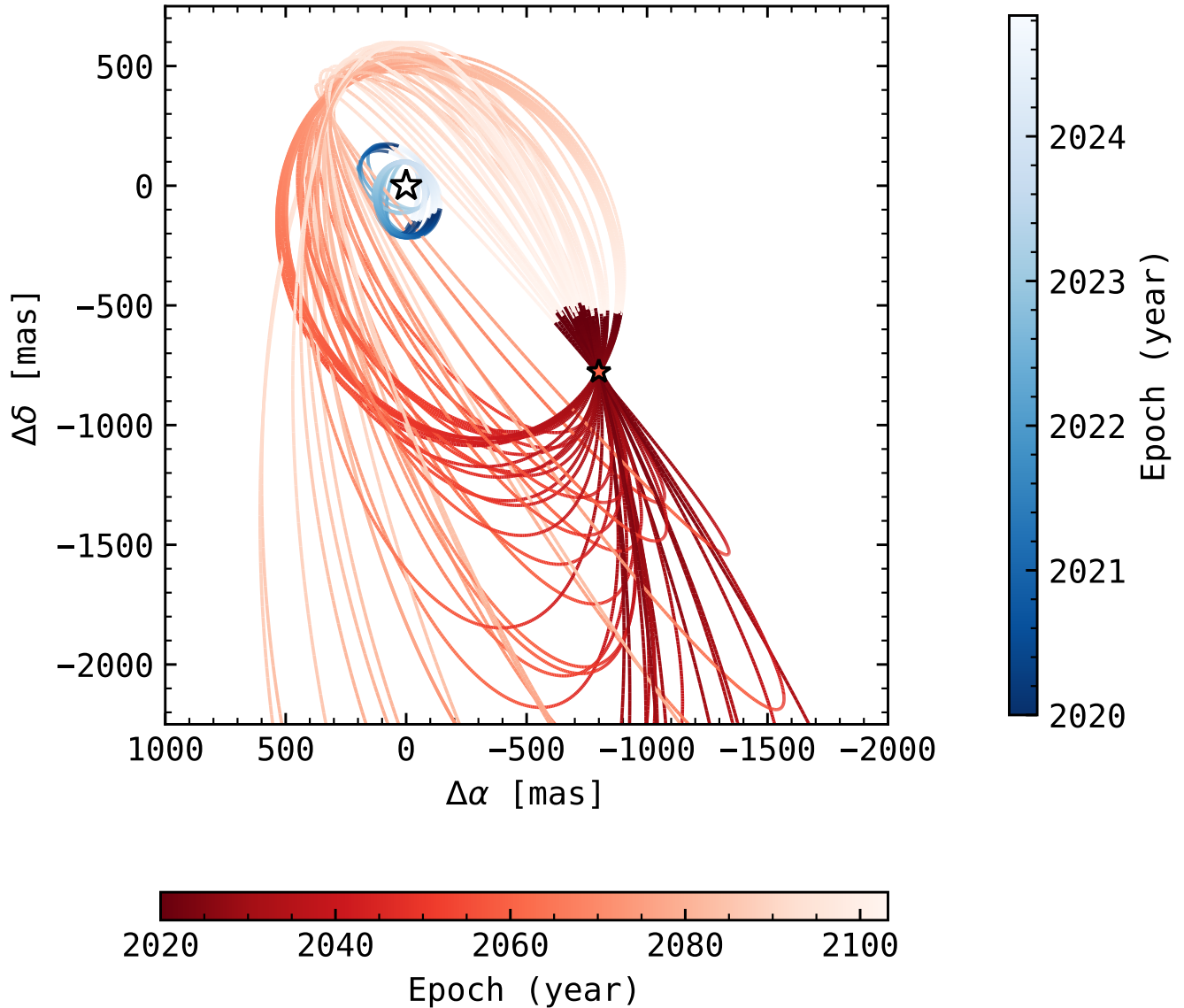


Figure 2. Sky projection of the architecture of the 14 Her system. The visual orbits for both planets, colored according to the time after the reference epoch 2020.0, MJD=58849.0. The new NIRCcam relative astrometry of 14 Her c strongly constrains the relative orientation of the two planets' possible orbital planes.

210 We use our new JWST relative astrometry of 14 Her c to update the orbital parameters of the system, combining
 211 this data set with literature RVs from the ELODIE (D. Naef et al. 2004), HIRES (L. J. Rosenthal et al. 2021), HRS
 212 (G. F. Benedict et al. 2023), and APF (S. S. Vogt et al. 2014) instruments spanning 25 years and absolute astrometry
 213 from Hipparcos and Gaia (T. D. Brandt 2018). We fit a total of 21 parameters with our 571 data points (3 from
 214 Gaia-Hipparcos absolute astrometry, 567 RV points, and 1 relative astrometry measurement from JWST) using two

publicly-available orbit fitting codes: `orvara`¹⁰ (T. D. Brandt et al. 2021) and `orbitize!`¹¹ (S. Blunt et al. 2020). Both of these orbit fitters use Bayesian inference with a Markov Chain Monte Carlo (MCMC) sampler to iteratively fit the data to Keplerian orbit models. Specifically, they use a Python implementation of a parallel-tempered version of the `emcee` (D. Foreman-Mackey et al. 2013) MCMC algorithm, namely `ptemcee` (W. Vousden et al. 2021). These two codes differ in their implementation of implicit priors, their treatment of parallaxes, their flexibility incorporating arbitrary absolute astrometry, and their computational speed.

Multi-planet systems are fit by iteratively solving two-body problems starting with the outermost companion. We used a Gaussian prior on the parallax of the star ($\pi=55.866 \pm 0.029$; (Gaia Collaboration et al. 2022)), a log-flat prior on the primary mass and RV jitters (one per instrument), uninformative priors on projections of the eccentricity, mean longitude, and ascending node, and a $\sin i$ prior on orbital inclination to give equal probability to all possible orbital orientations.

Our results with both orbit fitters use the same priors and data sets, and statistically agree on the accuracy and precision of the posterior probability distributions despite starting with different initial conditions and running for a different number of total steps, an indication that our results are robust and have converged. In Table 1, we present the results from the longest run starting with agnostic initial conditions with `orbitize!`. Details on the initial conditions and code setup for each orbit fitter can be found in the Appendix B.

Our measured relative astrometry of 14 Her c establishes the tangential direction of the reflex motion that the planet exerts on its host star, helping to apportion the contribution of each planet to the total acceleration of 14 Her between the Hipparcos and Gaia measurements. The visual orbits for the two planets are shown in Figure 2, and model fits to the stellar radial velocities are shown in Figure 8. Table 1 records a summary of orbital parameter values. The new orbital solution for planet c gives a mass of $M_c = 7.9_{-1.2}^{+1.6} M_J$, a semi-major axis of $a_c = 20.0_{-4.9}^{+12.0}$ au, and an eccentricity of $e_c = 0.52_{-0.12}^{+0.16}$, consistent with previous results (D. C. Bardalez Gagliuffi et al. 2021; F. Feng et al. 2022; G. F. Benedict et al. 2023). Two families of supplementary solutions for the inclination of 14 Her b arise from our orbit analysis: $i_b = 32.70_{-4.01}^{+7.45} \circ$ and $i_b = 146.90_{-9.74}^{+4.58} \circ$ driven by our lack of knowledge of the longitude of the ascending node for the inner planet (Ω_b), which dictates the direction of a planet’s motion along its orbit (as noted by F. Feng et al. 2024, for the case of 14 Her, either solution can be missed due to insufficient posterior sampling). Inclusion of HST/FGS observations (G. F. Benedict et al. 2023), and follow-up JWST astrometry of 14 Her c and/or future direct imaging of 14 Her b with the Nancy Grace Roman Space Telescope (T. D. Groff et al. 2021), will provide crucial additional constraints on the relative orientations of the orbits, helping to further resolve the architecture of the system.

3.2. Evolutionary and atmospheric modeling

Using our estimated dynamical mass for 14 Her c and the age posterior from the stellar characterization presented in (D. C. Bardalez Gagliuffi et al. 2021), we calculated fundamental parameters for the c planet with the `Sonora-Bobcat` cloudless substellar evolutionary models (M. S. Marley et al. 2021b), assuming a metallicity of $[Fe/H]=+0.5$, representative of the stellar metallicity (G. Gonzalez et al. 1999; R. E. Luck & U. Heiter 2006). We linearly interpolated across the publicly available model grid and predict $T_{\text{eff}}=300 \pm 30$ K, $\log(g)=4.25 \pm 0.15$, $R_{\text{pl}}=1.03 \pm 0.01 R_j$, $\log(L/L_{\odot})=-7.1 \pm 0.2$. Integrating the NIRCam/F444W flux for a `Sonora-Bobcat` atmospheric model with these parameters, we predict an apparent magnitude of 17.98 mag, which is 1.69 mag brighter than our observed apparent magnitude in F444W (see Section 2). Simultaneously fitting the `Sonora-Bobcat` atmospheric models to our F444W photometry and F200W limit, with T_{eff} as a free parameter and the other parameters fixed to their evolutionary values, we find $T_{\text{eff}}=210$ K. This ~ 90 K tension can be reasonably attributed to carbon disequilibrium chemistry driven by vertical mixing, the presence of ice clouds, an enhanced metallicity (K. J. Zahnle & M. S. Marley 2014a; B. Lacy & A. Burrows 2023) or some combination of these factors. Vertical mixing throughout the atmosphere can dredge up molecules that are formed at warm temperatures in the lower atmosphere and mix them into the cold, upper atmosphere faster than the chemical reaction timescale. This imbalance is most prominent among carbon and nitrogen molecules in objects colder than 500 K (K. J. Zahnle & M. S. Marley 2014a; B. Lacy & A. Burrows 2023). Carbon disequilibrium chemistry imparts deep CO and CO₂ absorption between 3 – 5 μm (B. E. Miles et al. 2020; S. A. Beiler et al. 2023, 2024a) in the spectra of substellar objects, even though the dominant carbon species at these temperatures should be CH₄ in chemical equilibrium (B. Lacy & A. Burrows 2023; K. J. Zahnle & M. S. Marley 2014a). Clouds made of water ice

¹⁰ <https://github.com/t-brandt/orvara>

¹¹ <https://orbitize.readthedocs.io/en/latest/>

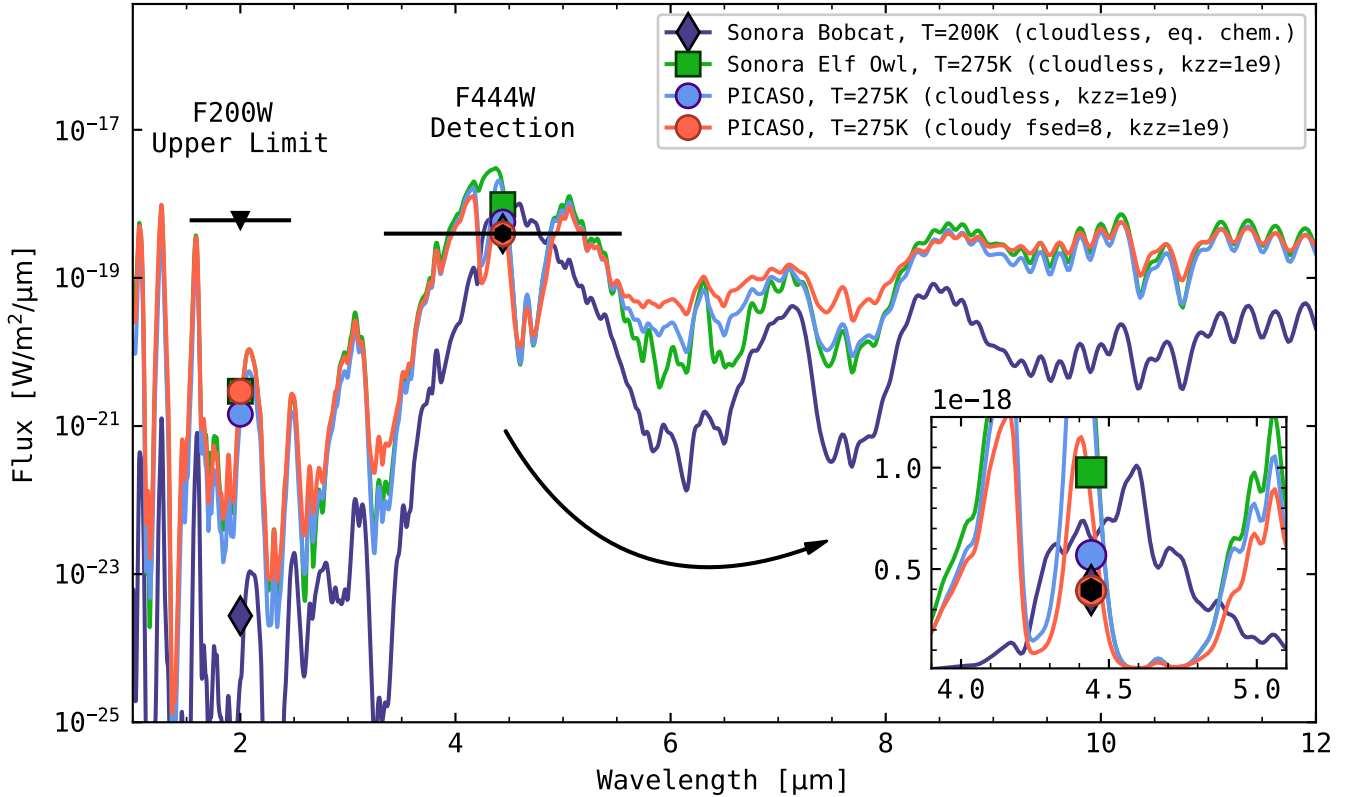


Figure 3. Carbon disequilibrium chemistry and water clouds are likely in 14 Her c’s atmosphere. JWST/NIRCam photometry of 14 Her c (F444W flux as a black hexagon, F200W upper limit as a black triangle) compared to atmospheric model spectra (colored lines) integrated over the filter bandpasses (colored circles, squares, diamonds). Publicly available Sonora Bobcat (M. S. Marley et al. 2021a) and Sonora Elf Owl (S. Mukherjee et al. 2024b) models (in dark blue and green, respectively) are unable to reproduce the data with temperatures in agreement with evolutionary model predictions. Custom PICASO models with an updated treatment of carbon disequilibrium chemistry (light blue) brings the models in better alignment with the observations and evolutionary model predictions. Adding water ice clouds (red) to these custom atmospheric models brings the observations into agreement at 1σ with both the atmospheric and evolutionary models.

particles can also absorb or scatter outbound light, and redistribute it to different wavelengths. To explore the effects of carbon disequilibrium chemistry and cloud formation on our measured F444W photometry, we generated a custom mini-grid of atmospheric models matching the metallicity of the star ($[\text{Fe}/\text{H}] = +0.5$), assuming a solar C/O, and including disequilibrium chemistry and water ice clouds based on the Sonora Elf Owl family of models (S. Mukherjee et al. 2024b). Details are described in Appendix C.

Figure 3 shows that our JWST photometry in F444W is consistent with a cloudy atmosphere with carbon disequilibrium chemistry driven by strong vertical mixing (B. E. Miles et al. 2020; S. A. Beiler et al. 2023, 2024a) at $T_{\text{eff}} = 275\text{K}$ and $\log g = 4.25$. This result puts 14 Her c in the running for the coldest directly imaged exoplanet to date, a title currently held by Epsilon Indi Ab (E. C. Matthews et al. 2024a). Although these two planets have not yet both been imaged at equivalent wavelengths, the mid-infrared color of Epsilon Indi Ab similarly suggests a temperature of $T_{\text{eff}} = 275 - 300\text{K}$.

3.3. Dynamical simulations

We explored the present-day dynamical evolution of the system by performing secular (i.e. orbit-averaged) three-body simulations using the publicly available *KozaiPy* software¹². *KozaiPy* solves the equations of motion for three-body hierarchical systems ($a_b \ll a_c$) presented in P. P. Eggleton & L. Kiseleva-Eggleton (2001); D. Fabrycky & S. Tremaine

¹² <https://github.com/djmunoz/kozaipy>

(2007) to octupole order $(a_b/a_c)^3$ (S. Naoz et al. 2013). These packages include effects from equilibrium tides and general relativity, but as both planets are relatively far from the host star, such short-range effects are not impactful. In this limit, the semimajor axes of both planets remain fixed while mutual gravitational perturbations cause the eccentricities and inclinations to oscillate. We note that this level of approximation is strictly valid only for an inner test particle influenced by a massive, arbitrarily eccentric external perturber, and as such may not fully capture some relevant dynamics in the 14 Her system due to its similarly massive planets. There is no existing analytic prescription describing this regime, which is typically probed with direct N -body simulations (J. Teysandier et al. 2013). We reserve detailed exploration of this for future work.

We sampled $\sim 10,000$ parameter vectors from the posterior distribution derived from `orbitize!` and integrated them forward in time 10 Myr, tracking the evolution of the orbital elements of both planets using orbit-averaged simulations assuming a hierarchical approximation ($a_b \ll a_c$). All orbital solutions show substantial eccentricity and inclination oscillations for both planets as a result of strong secular perturbations. Figure 5 shows the distribution of the eccentricity oscillation amplitude of 14 Her b $\Delta e_b \equiv \max e_b - \min e_b$, as well as examples of two representative simulations – one characterized by moderate eccentricity and inclination oscillations, and one by much stronger oscillations.

4. DISCUSSION

4.1. On the mutual inclination of the 14 Her planets

With our new orbital solutions, we revise the mutual inclination angle Θ between the two orbital planes, defined as

$$\cos \Theta = \cos i_b \cos i_c + \sin i_b \sin i_c \cos(\Omega_b - \Omega_c)$$

in e.g., D. C. Bardalez Gagliuffi et al. 2021; I. Czekala et al. 2019. This results in a bimodal posterior distribution of mutual inclinations of $\Theta = 32_{-15.1}^{+13.6} \text{ }^\circ$ and $\Theta = 145.0_{-11.1}^{+15.8} \text{ }^\circ$, for i_b greater than or less than 90° , respectively. These values represent roughly a factor of two improvement in precision compared to the previous estimate of the mutual inclination before our relative astrometry measurement of 14 Her c with JWST ($\Theta = 96.3_{-29.1}^{+36.8} \text{ }^\circ$, D. C. Bardalez Gagliuffi et al. 2021). The nonzero mutual inclination between the orbits of 14 Her b and c and large eccentricities are in stark contrast with the planets in our own Solar System, as well as younger, directly imaged multiplanet systems like HR 8799 (C. Marois et al. 2008), β Pictoris (A. M. Lagrange et al. 2010), and HD 206893 (S. Hinkley et al. 2023) that have multiple planets on (roughly) coplanar, low eccentricity orbits (B. P. Bowler et al. 2020).

4.2. Potential for disequilibrium chemistry in the atmosphere of 14 Her c

14 Her c is over a million times fainter than its host star at $4.4 \mu\text{m}$ (a contrast of $9.6 \pm 0.5 \times 10^{-7}$, see Figure 6), and roughly one magnitude fainter than the coldest isolated brown dwarf known, WISE J0855–0714 (M. J. Rowland et al. 2024) in the comparable Spitzer filter centered at $4.5 \mu\text{m}$. The 90 K degree tension between the temperatures from evolutionary and spectral models is $> 3\sigma$ significant, suggesting the presence of additional sources of $4.4 \mu\text{m}$ opacity in the planet’s atmosphere such as clouds or disequilibrium chemistry.

Our custom model fits imply that 14 Her c should have a deep CO_2 absorption feature at $4.2 \mu\text{m}$ (S. A. Beiler et al. 2024b), which can be tested using follow-up JWST coronagraphic images with narrower bandwidth filters (W. O. Balmer et al. 2025). Similarly, our photometry implies that other cold planets like 14 Her c are likely slightly fainter at $4.4 \mu\text{m}$ than expected for their mass and age. Future JWST observations of 14 Her c with multi-band photometry across the near and mid-infrared could feasibly quantify the thermal emission, cloud opacity slope, and CO_2 , CO, and NH_3 absorption feature strengths predicted by these models. Direct spectroscopy with JWST may be able to further refine the molecular abundances in the planet’s atmosphere, although this will be challenging due to the planet’s high contrast. These observations would provide the first glimpses into the complexity of this field-age, giant exoplanet atmosphere as a benchmark for other cold exoplanets and Y-type brown dwarfs, yielding new insights into the physics and chemistry occurring in low temperature giant planet atmospheres.

4.3. A cold planet in a dynamically hot system

The unusual present configuration of this system is not representative of most observed multi-planet systems and instead points to past and ongoing dynamical interactions. The results from our dynamical simulations (see Section 3.3) indicate that both planets in the 14 Her system are currently experiencing significant secular eccentricity and inclination

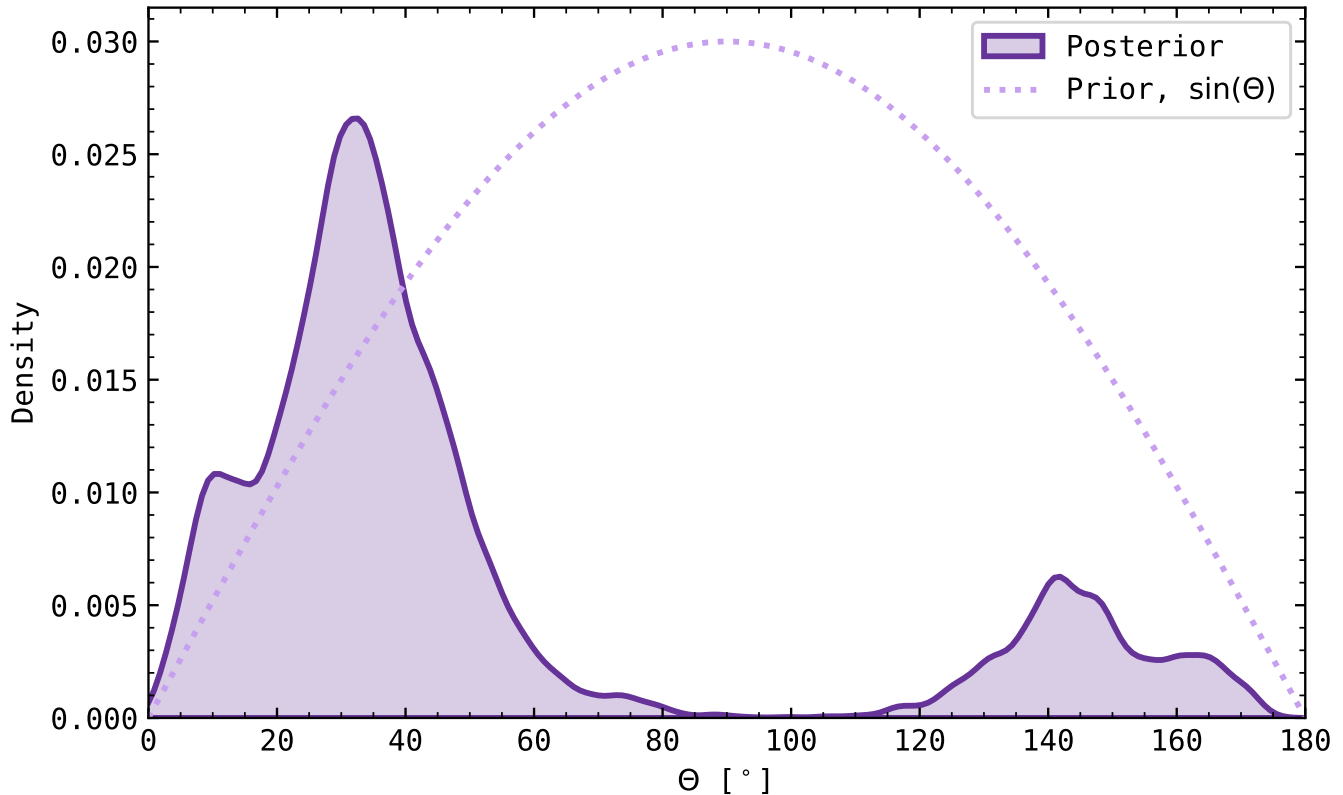


Figure 4. The posterior distribution of mutual inclination angles Θ between the orbits of 14 Her b and c, compared to the Sine prior. The constraint on the mutual inclination is driven by the likelihood function and not the prior.

oscillations. While it is impossible to directly compare the magnitude of these excursions to the exoplanet population at large (as such comprehensive detailed dynamical modeling does not exist for all systems), an illustrative comparison can be made with the Solar System. The largest amplitude eccentricity excursions experienced by a Solar System planet are of order ~ 0.1 by Mercury, whereas 14 Her b, on average, experiences oscillations with nearly five times this amplitude. This behavior makes 14 Her the only currently known dynamically “hot” multi-planet system with an imaged planet¹³. However, even though the orbital parameters vary periodically, the system is stable on this timescale.

Planet-planet scattering, including a planetary ejection, was proposed as a potential hypothesis to explain the origin of this peculiar system architecture (D. C. Bardalez Gagliuffi et al. 2021). With our new orbital constraints, future N-body simulations exploring this and other initial scenarios will be key to gauge the feasibility of this mechanism in shaping the configuration of this system and its relative occurrence among the long-period exoplanet population. Ejections of giant planets may then be a common avenue to produce the observed population of “rogue” planets in our galaxy (T. Sumi et al. 2023).

5. CONCLUSIONS

In this letter we present the first direct images of 14 Her c. The key takeaways of our study are as follows:

1. Coronagraphic imaging of 14 Her with JWST/NIRCam achieved deep contrasts ($< 10^{-6}$) at thermal wavelengths ($4.5 \mu\text{m}$) and spatial scales between 15-150 au. These observations detected the known planet 14 Her c at $> 5 \sigma$ confidence.

¹³ For example, the dynamically “cold” directly imaged multi-planet system β Pictoris bc likely experiences secular eccentricity oscillations of order $\Delta e < 0.2$ (S. Lacour et al. 2021), and the HR 8799 bcde system likely experiences oscillations of order $\Delta e < 0.05$ (J. J. Wang et al. 2018).

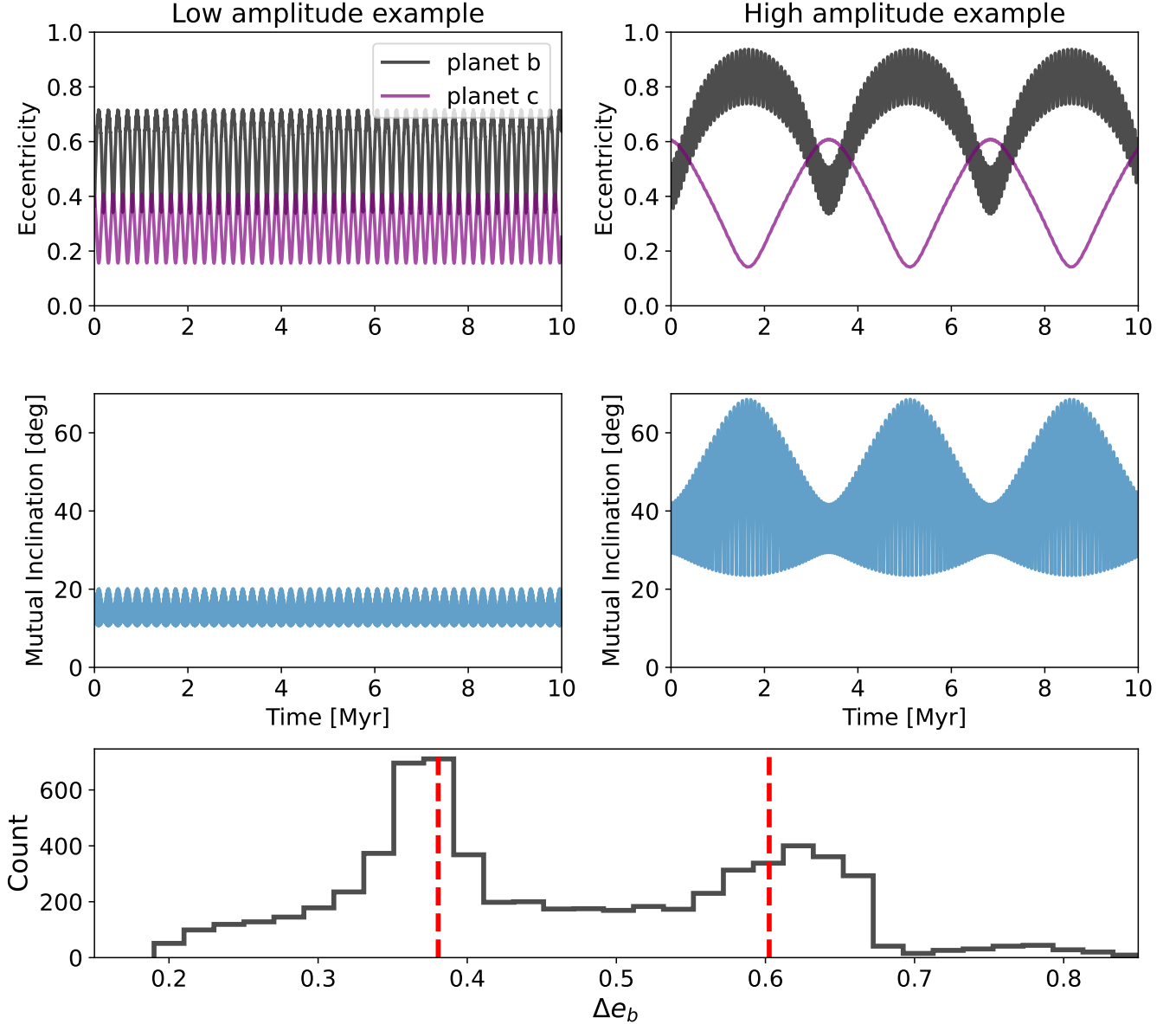


Figure 5. Example dynamical simulations, initialized from different parameter vectors from the `orbitize!` posterior distribution. The left and right columns show examples of lower and higher amplitudes of secular oscillations, as seen in the eccentricity variations of both planets and the mutual inclination variations. The histogram in the bottom panel shows the distribution of Δe_b across all simulations, and the values corresponding to the two example simulations are shown with the vertical red lines.

- 341 2. The planet appears within 1σ of its predicted location from orbits fit to previous absolute astrometry and radial
 342 velocity measurements. The probability of a chance alignment with a background source are negligible compared
 343 to the likelihood the source is 14 Her c.
- 344 3. 14 Her c ($T_{\text{eff}} \sim 275\text{--}300\text{ K}$) rivals ϵ Indi Ab ($\sim 275\text{--}300\text{ K}$, [E. C. Matthews et al. 2024b](#)) and TWA 7 b ($\sim 315\text{ K}$,
 345 [A. M. Lagrange et al. 2025b](#)) as one of the coldest planets yet directly imaged, and with ϵ Indi Ab ($\sim 3.5\text{ Gyr}$,
 346 [E. C. Matthews et al. 2024b](#)) as one of the oldest ($\sim 4.6\text{ Gyr}$).
- 347 4. Temperature estimates for 14 Her c disagree slightly within 90 K or 1σ between the estimate from dynamical
 348 mass and age and that from the F444W photometry. This tension between estimates could be explained by

the presence of carbon disequilibrium chemistry and/or water ice clouds in the atmosphere. See Figure 3 for atmospheric modeling.

5. The misalignment between orbits identified in D. C. Bardalez Gagliuffi et al. (2021) remains. With our new detection, we have refined the parameters of both planetary orbits in the system and constrained the misalignment more precisely. Only five other multi-planet systems with measured orbits exhibit a significant misalignment, and so far 14 Her is the only one with a directly imaged planet.
6. The unusual system architecture of 14 Her c is suggestive of dramatic past and present dynamical interactions. Our preliminary dynamical simulations indicate ongoing secular eccentricity and inclination oscillations with large eccentricity excursions roughly 5 times those of Mercury.

This system is a unique benchmark to describe the dynamical evolution of multi-planet systems and the atmospheric properties of Jupiter analogs. Future multi-band imaging or cross correlation spectroscopy with JWST can provide a glimpse into the spectral energy distribution and the atmospheric composition of this planet. 14 Her is an exciting target for the Coronagraphic Instrument aboard the Roman Space Telescope. Precisely constraining the location of the inner planet will establish both planetary orbits in the system, the degree of orbital misalignment, and exclude a subpopulation of orbital solutions to improve our knowledge on the ongoing dynamical interactions of the system.

ACKNOWLEDGMENTS

We thank an anonymous reviewer for their review, which improved the quality of this manuscript. D.B.G., W.O.B, and M.G. acknowledge support from Space Telescope Science Institute JWST grant No. JWST-GO-03337. J.M. is supported by the NSF Graduate Research Fellowship. This work was performed in part using high-performance computing equipment at Amherst College obtained under National Science Foundation (NSF) Grant No. 2117377. Part of this work was carried out at the Advanced Research Computing at Hopkins (ARCH) core facility (rockfish.jhu.edu), which is supported by the National Science Foundation (NSF) Grant No. OAC1920103.

W.O.B. thanks E. Bogat, J. I. Adams Redai, R. Bendahan-West, R. Ferrer-Chavez, A. James, and R. Kane for helpful discussions.

AUTHOR CONTRIBUTIONS

D.B.G. and W.O.B. planned and proposed the James Webb Space Telescope observations, led the collaboration, and wrote the manuscript. W.O.B. and L.P. led the JWST image processing, starlight subtraction, photometric and astrometric measurements. D.B.G., W.O.B., M.G., and T.D.B. led the orbit fitting with both `orvara` and `orbitize!`. D.B.G., W.O.B. estimated fundamental parameters with evolutionary models. S.M., T.L., M.R., B.B. designed and ran secular dynamical simulations. J.M., C.M., B.L. developed a mini-grid of atmospheric models and fit the measured JWST photometry to them. J.G. advised on observation planning for the NIRCcam coronagraph. E.C.M., A.C., B.P.B., J.F., C.F., E.R. provided comments and expertise throughout the analysis.

Facilities: JWST(NIRCcam), OHP:1.93m(ELODIE), Keck:I(HIRES), Smith(Cross-Dispersed Echelle Spectrograph), APF, HIPPARCOS, Gaia

Software: `astropy`, `pyKLIP`, `spaceKLIP`, `orbitize!`, `orvara`, `KozaiPY`, `PICASO`

APPENDIX

A. IMAGE REDUCTION

The uncalibrated Stage 0 (*uncal.fits) data products were acquired from the Barbara A. Mikulski Archive for Space Telescopes (MAST) ¹⁴ and processed with `spaceKLIP`¹⁵, a community developed pipeline for high contrast imaging

¹⁴ The data described here may be obtained from the MAST archive at [doi:10.17909/gx61-s247](https://doi.org/10.17909/gx61-s247)

¹⁵ <https://spaceklip.readthedocs.io/en/latest/>

with JWST (J. Kammerer et al. 2022). `spaceKLIP` wraps the `rwst` pipeline (H. Bushouse et al. 2023) for basic data processing steps with modifications for coronagraphic imaging reduction. Data reduction via `spaceKLIP` for observations using the F444W filter and MASK335R coronagraph has been described at length (J. Kammerer et al. 2022; A. L. Carter et al. 2023; K. Franson et al. 2024b; J. Kammerer et al. 2024; W. O. Balmer et al. 2025). We used `spaceKLIP` v2.1, via github commit #11df3a1, and `rwst` v1.18; the calibration files were from CRDS v12.1.5 and the `rwst_1364.pmap` CRDS context¹⁶. Briefly, the data were fit “up the ramp” using the “Likely” algorithm described in (T. D. Brandt 2024a,b) and transformed from Stage 0 images into Stage 2 (`*calints.fits`) images, using a jump threshold of 4 and 4 pseudo-reference pixels on all sides of the subarrays; this process collates the frames (non-destructive reads and averages of the detector) into integrations, which end with destructive readouts of the detector, while using the differences between groups to correct for cosmic rays and other artifacts. The 1/f noise typical of thermal imaging with HgCdTe arrays was mitigated using a median filter computed along each column. We skipped dark current subtraction following (A. L. Carter et al. 2023). Pixels flagged by the `rwst` pipeline as well as 5σ outliers detected post facto using sigma clipping were replaced with a 2-dimensional interpolation based on a 9-pixel kernel. We also identified additional pixels affected by cosmic rays by flagging pixels with significant temporal flux variations across integrations and replaced them by their temporal median. Subsequently, the images were blurred above the Nyquist sampling criterion, using a Gaussian with a FWHM of 2.70 for the F444W/LW detector and 2.77 for the F200W/SW detector. These values ensure that sharp features in the data do not create artifacts when Fourier shifts are applied to the undersampled images. The position of the star behind the coronagraph was estimated by fitting a model coronagraphic PSF from `webbpsf_ext`¹⁷ to the first science integration. All subsequent images were shifted by this initial offset. Images were cross-correlated to the first science integration, and these small shifts were applied to each integration to center the entire observing sequence to the first science integration. The recovered shifts were equivalent to and reproduced the small grid dither sequence that was commanded.

A.1. Starlight subtraction and contrast estimation

The residual starlight in the coronagraphic images was modeled and removed using the Karhunen–Loève Image Projection (KLIP) algorithm (R. Soummer et al. 2012) through the Python implementation `pyKLIP`¹⁸ (J. J. Wang et al. 2015) wrapped by `spaceKLIP`. This algorithm uses Principal Component Analysis (PCA) to create an orthogonal basis set of eigenimages from the reference images. The science images are projected onto this basis to isolate and remove the contribution from the stellar PSF common between the reference and science images. This can be done on annular or radial subsections of the data by specifying a number of `annuli` and `subsections` in which to split the data, while the number of eigenimages used to construct the PSF model are specified with the `numbasis` parameter (sometimes referred to as the number of “KL modes”).

We used ADI and RDI to create our model PSF and subtracted the starlight with `annulus=1`, `subsections=1`, and `numbasis` ∈ [1, 2, 3, 4, 5, 6, 7, 8, 9, 10, 25, 50, 100]. In the F200W filter, an extended source (a background galaxy) is visible in all KL modes at a separation of 1''5 to the SE, and becomes very apparent by the 6th KL mode. In the F444W filter, this same galaxy appears by the 5th KL mode subtraction, and another source, a point source, becomes apparent to the SW. By the 10th KL mode, most other speckles in the image have been suppressed, leaving the galaxy at 1''5 to the SE in both filters, a few faint, extended sources beyond 2''0 (one at 4''0 to the NE, and one at 8''9 to the N), and the point source to the SW in F444W. We detected no other point sources in either filter. We verified that the point source appears in both roll angles and rotates with the astrophysical scene, not the detector frame. The signal-to-noise ratio of the source climbs from <1 to 5.7 between `numbasis` 1 and 5, and plateaus about this value for `numbasis` > 5. We tested the robustness of the source to the starlight subtraction by varying KLIP parameters, and found that the point source persists for `annuli` ∈ [2–16] and `subsections` ∈ [2–8], `numbasis` > 5. The significance of the source does not vary dramatically with the choice of KLIP parameter, but is greatest for the simplest, least “aggressive” choice in parameters, `annuli=1`, `subsections=1` because there is the least self-subtraction for these parameters (J. I. Adams Redai et al. 2023). We also verified that the source persists, albeit at lower SNR, in subsets of the science integrations; we were able to detect the source at $\gtrsim 4\sigma$ in up to a third of the total dataset, regardless of which frames were selected. Since the contrast and position of the point source agrees well with the mass and position predicted for the epoch of observation based on orbits for 14 Her c from (D. C. Bardalez Gagliuffi et al. 2021) and (G. F. Benedict et al.

¹⁶ https://jwst-crds.stsci.edu/display_context_history/

¹⁷ https://github.com/JarronL/webbpsf_ext

¹⁸ <https://pyklip.readthedocs.io/en/latest/>

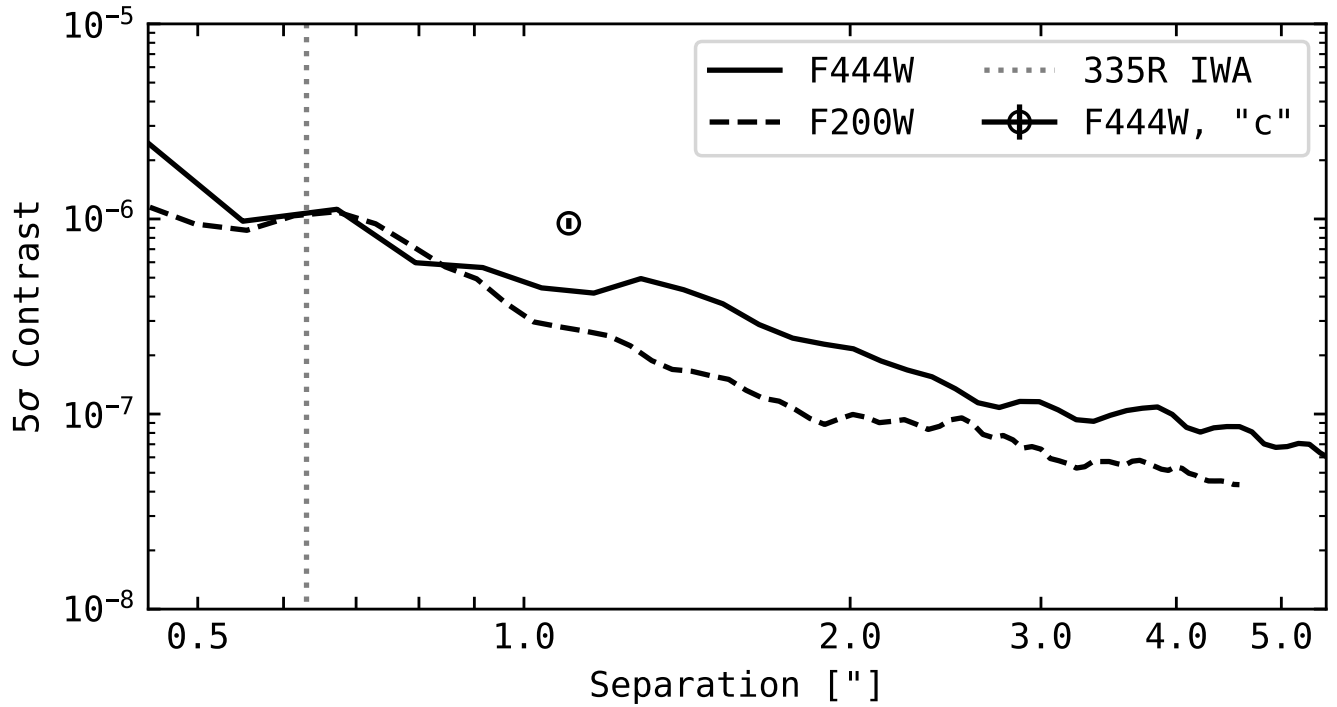


Figure 6. Contrast curve for the NIRCam observations of 14 Her using the 335R coronagraph. The F444W and F200W 5σ contrast curves are shown as solid and dashed lines respectively. The likely detection of 14 Her c at $\sim 1''.1$ is plotted as an black circle and error bar. The nominal 335R inner working angle (“IWA”), where the coronagraph transmission reaches 50%, is indicated by a vertical dashed line. *Takeaway:* Our detection of 14 Her c is statistically significant.

2023), we proceed to estimate its astrometry and photometry using the `annuli=1, subsections=1, numbasis=25` PSF subtracted images (Figure 1).

A.2. Forward model subtraction of both sources

The forward modeling of the point source, 14 Her c, is described in §2.1. In this section, we briefly describe a simplistic forward model for the extended source, the background galaxy, in the F444W filter and present the residual images for the forward modeling. The procedure for modeling the extended source follows from the point source forward model, except that at each step the `webbpsf` model is convolved with a 2D Gaussian parameterized by a FWHM in the x and y directions and a correlation term θ . This model does not fully capture the structure of the source, as residuals are apparent to the SE of the central source, but serves to describe it at first order. Figure 7 illustrates the F444W image (Figure 1), the same image with the background galaxy subtracted, and with both sources subtracted.

B. ORBIT FITTING

B.1. *orvara*

For an initial `orvara` run, we used all three datasets with 100 walkers over 30 temperatures, 1 million steps per walker (i.e., 500,000 steps for each planet) and saved every 50th step for inference, starting with the median parameter values from the posteriors published in (D. C. Bardalez Gagliuffi et al. 2021) as initial conditions. We constrained the RV jitter for each instrument to a $10^{-5} - 10$ m/s range. The total chain length per walker was 20,000 out of which the first 500 steps were discarded as burn-in.

The single epoch of JWST relative astrometry for the 14 Her c planet helped to strongly constrain its orbital parameters. However, our lack of constraint on the longitude of the ascending node for 14 Her b produced a bimodal distribution for its orbital inclination. About 2/3 of the orbit posteriors were consistent with an inclination of b lower than 90° , whereas the remaining 1/3 of orbits had inclinations for b greater than 90° . To explore this degeneracy, we ran new orbit fits to produce longer chains of 3 million steps per walker divided evenly over the two planets, using

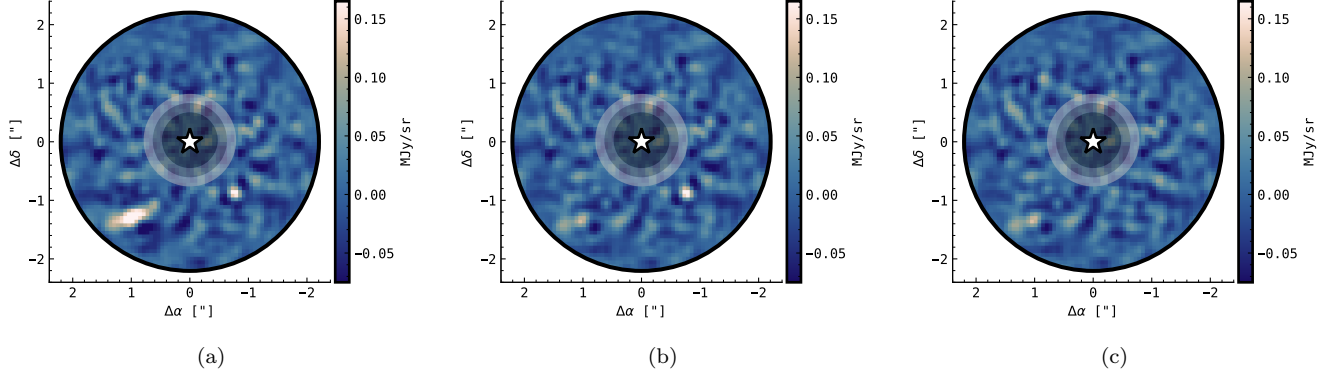


Figure 7. Forward modeling of sources in the NIRCam F444W image. (a) Reproduction of the PSF subtracted image in Figure 1. The two prominent sources are an extended source (a galaxy) to the SE and a point source (14 Her c) to the SW. (b) The residuals after the subtraction of a simple forward model of the background galaxy, a `webbpsf` point source convolved by a 2D Gaussian. Small (10%) residuals to the SE of the center of the galaxy are apparent. The visual significance of 14 Her c is apparent, as the galaxy has been suppressed. (c) The residuals of the image after the point source forward model for 14 Her c has been subtracted.

459 100 walkers over 30 temperatures. On separate runs, we tried each family of inclinations for b and the associated
 460 parameters for b and c as initial conditions. The total chain length used for inference on each run had 60,000 steps
 461 with 3000 steps discarded as burn-in, both with a mean acceptance fraction of 0.029.

462 It appears as if the initial run with 1 million steps had not yet converged and based on the starting conditions, which
 463 initialized at an inclination of $32.7_{-5.3}^{+3.2}$ ° for b (D. C. Bardalez Gagliuffi et al. 2021), gave preference to this family of
 464 solutions while only starting to explore the family of supplementary inclinations greater than 90°. The subsequent
 465 longer runs reversed the proportion of orbits of 14 Her b with each inclination, with only 1/5 of posteriors consistent
 466 with a $i_b < 90^\circ$ regardless of the initial conditions of b inclinations (i.e., below or above 90°).

467 B.2. *orbitize!*

468 We corroborated our results with an independent orbit fit using `orbitize!`. We set normally distributed priors on
 469 the host star mass ($M_* = 0.98 \pm 0.04$; (D. C. Bardalez Gagliuffi et al. 2021)) and the system parallax ($\pi = 55.866 \pm 0.029$;
 470 (Gaia Collaboration et al. 2022)). We adopted uniform priors between -5 and 5 km/s for the RV zero points, and log
 471 uniform priors between 10^{-5} and 10^2 km/s for the RV jitter nuisance parameters. We restrict the semi-major axes for
 472 the inner and outer planets not to cross, placing log-uniform priors between 0.1 and 5 au for the inner, and between 5
 473 and 500 au for the outer. Similarly, we place log-uniform priors on the planet masses ranging from 0.2 to 20 Jupiter
 474 masses. We adopted uninformative priors on the eccentricity and the angles describing the visual orbital elements for
 475 the two planets (Table 1; (S. Blunt et al. 2020)).

476 For our `orbitize!` run we use 100 walkers (initialized randomly within the prior space) over 20 temperatures and
 477 2.5×10^6 steps. We discarded the first 2.25×10^6 steps as burn-in and thinned the sampler by a factor of 10, saving only
 478 every 10^{th} step, resulting in a final posterior distribution with 2.5×10^6 orbits, each composed of 26 parameters. The
 479 fit yields two modes in the posterior distribution on i_b and Ω_b , due to a degeneracy in the visual orbit of the inner
 480 planet b, while the mode of the parameters describing the orbit of c all have a tail of solutions that are correlated
 481 with the RV jitter terms, due to the fractional phase coverage of the planet’s orbit by each instrument. Even after
 482 the exhaustive MCMC run, the two modes are not equivalently weighted, and the solutions with $i_b = 147_{-9.68}^{+4.57}$ °
 483 are more numerous, at a ratio of about 3 to 1, compared to the solutions with $i_b = 32.46_{-4.25}^{+7.31}$ °. This results in a
 484 posterior distribution of mutual inclinations of $\Theta = 32_{-15.1}^{+13.6}$ ° and $\Theta = 145.0_{-11.1}^{+15.8}$ °, for i_b greater than or less than
 485 90°, respectively. We adopt this set of posterior parameters and present the median and 1σ confidence intervals of the
 486 marginalized posterior distribution in Table 1. Figure 8 visualizes the radial velocity measurements compared to 100
 487 randomly drawn posterior models, and Figure 2 shows the sky-projected visual orbits for both planets on the same
 488 scale. Figures 9 and 10 show the posterior distribution on the orbital elements for 14 Her b and c respectively, without
 489 the nuisance parameters.

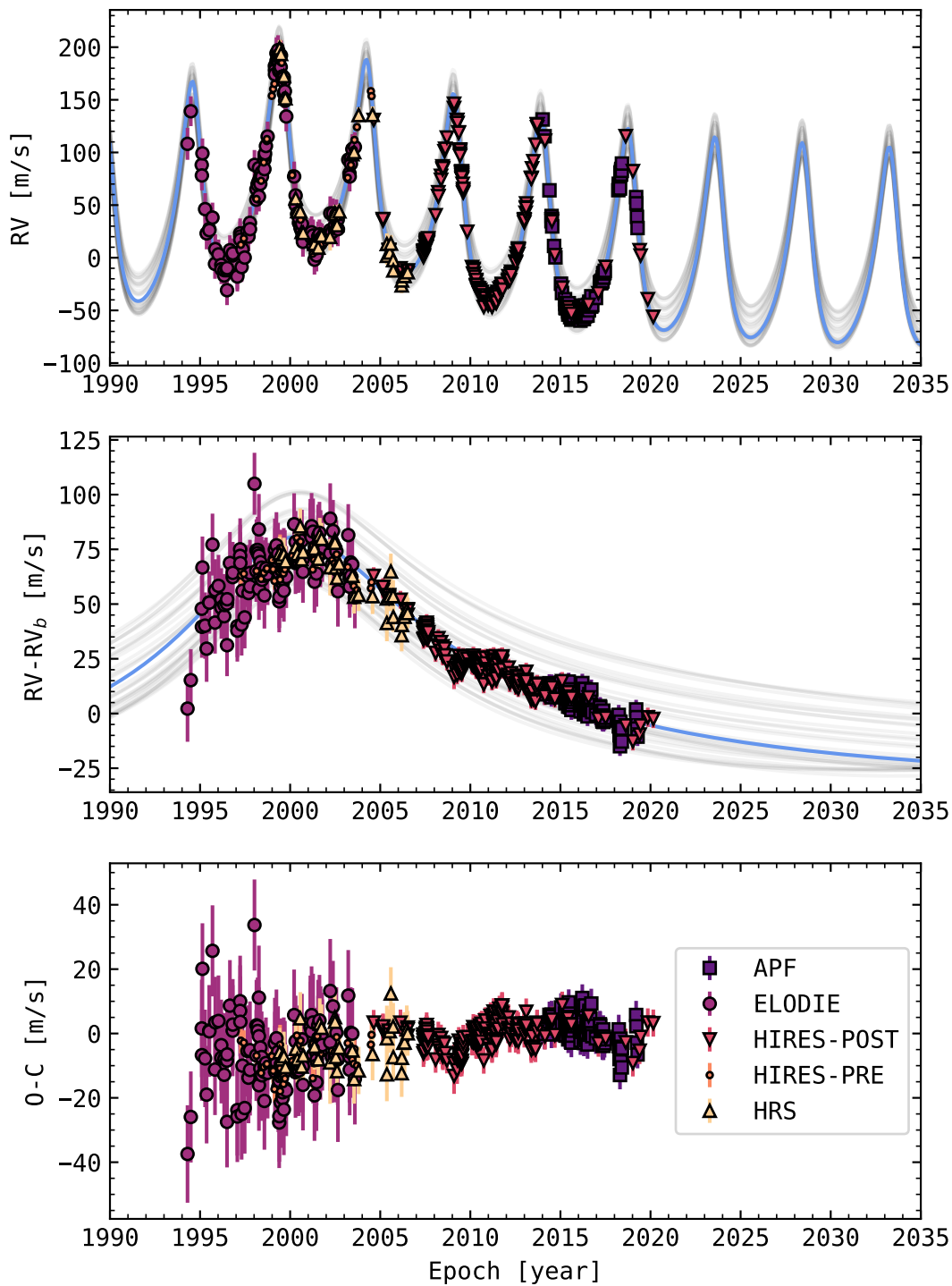


Figure 8. The stellar radial velocities driven by the orbits of both planets, as measured by various instruments. The ~ 5 yr modulation from 14 Her b is apparent, as is the long term variation due to 14 Her c, although there is not complete coverage of the outer planet’s orbit.

Parameter	Description	Units	Prior	Max. A-posteriori	Median and 68% CI
a_b	Semi-major axis	au	Log-uniform [0.1, 5]	2.839	$2.839^{+0.039}_{-0.041}$
e_b	Eccentricity	...	Uniform [0,1]	0.3683	$0.3683^{+0.0029}_{-0.0029}$
i_b	Inclination	degree	Sine [0,180]	147.8	$146.7^{+4.584}_{-9.740}$
i_b^*	Inclination	degree	Sine [0,180]	29.79	$32.66^{+7.448}_{-4.011}$
Ω_b	Longitude of the Ascending Node	degree	Uniform [0,360]	202.7	$197.8^{+4.240}_{-5.615}$
Ω_b^*	Longitude of the Ascending Node	degree	Uniform [0,360]	44.12	$44.69^{+3.438}_{-4.011}$
τ_b	Relative Periastron \ddagger	...	Uniform [0,1]	0.7670	$0.7672^{+0.0013}_{-0.0013}$
a_c	Semi-major axis	au	Log-uniform [5, 500]	15.1	$20.0^{+12.0}_{-4.9}$
e_c	Eccentricity	...	Uniform [0,1]	0.40	$0.52^{+0.16}_{-0.12}$
i_c	Inclination	degree	Sine [0,180]	114.0	$116.3^{+24.64}_{-9.167}$
ω_c	Argument of periastron \dagger	degree	Uniform [0,360]	173.0	$172.5^{+4.011}_{-4.584}$
Ω_c	Longitude of the Ascending Node	degree	Uniform [0,360]	206.8	$205.1^{+7.448}_{-10.31}$
τ_c	Relative Periastron \ddagger	...	Uniform [0,1]	0.66	$0.78^{+0.11}_{-0.12}$
π	Parallax	mas	$\mathcal{N}(55.866, 0.029)$	55.871	$55.866^{+0.028}_{-0.029}$
γ_{APF}	RV ZP	km/s	Uniform	0.044	$0.031^{+0.013}_{-0.017}$
σ_{APF}	RV jitter	km/s	Log-uniform	0.00345	$0.00347^{+0.00027}_{-0.00023}$
γ_{ELODIE}	RV ZP	km/s	Uniform	-0.028	$-0.041^{+0.013}_{-0.017}$
σ_{ELODIE}	RV jitter	km/s	Log-uniform	0.007	$0.007^{+0.001}_{-0.001}$
$\gamma_{\text{HIRES-POST}}$	RV ZP	km/s	Uniform	-0.0041	$-0.017^{+0.013}_{-0.016}$
$\sigma_{\text{HIRES-POST}}$	RV jitter	km/s	Log-uniform	0.0031	$0.0031^{+0.0002}_{-0.0002}$
$\gamma_{\text{HIRES-PRE}}$	RV ZP	km/s	Uniform	0.0032	$-0.010^{+0.013}_{-0.017}$
$\sigma_{\text{HIRES-PRE}}$	RV jitter	km/s	Log-uniform	0.0027	$0.0028^{+0.0004}_{-0.0004}$
γ_{HRS}	RV ZP	km/s	Uniform	-0.032	$-0.045^{+0.013}_{-0.017}$
σ_{HRS}	RV jitter	km/s	Log-uniform	3.9e-05	$0.00015^{+0.00084}_{-0.00013}$
\mathcal{M}_b	Mass of b	M_J	Log-uniform [0.2,20]	9.2	$8.9^{+1.3}_{-1.7}$
\mathcal{M}_c	Mass of c	M_\odot	Log-uniform [0.2,20]	7.5	$7.9^{+1.6}_{-1.2}$
\mathcal{M}_A	Mass of A	M_\odot	$\mathcal{N}(0.98, 0.04)$	0.965	$0.97^{+0.04}_{-0.04}$
Θ	Mutual inclination	degree	...	31.51	$32.09^{+13.75}_{-14.90}$
Θ^*	Mutual inclination	degree	...	141.5	$145.0^{+16.04}_{-10.89}$

Table 1. Orbit fit results. The results of the longest MCMC run using `orbitize!` was adopted here. * $i_b < 90^\circ$ mode solutions for the orbit of b, with roughly 3 to 1 probability compared to the mode containing $i_b < 90^\circ$ solutions. \dagger The argument of periastron of the planet’s orbit, not the star’s orbit, about the center of mass. \ddagger Defined as $\tau = \frac{t_p - t_{\text{ref}}}{P}$, where t_p is the time of periastron passage and $t_{\text{ref}} = 58849.0$ MJD.

C. ATMOSPHERIC MODELING

We compute custom atmospheric models using `PICASO` (N. E. Batalha et al. 2019; S. Mukherjee et al. 2023), an open-source Python-based framework that solves for one-dimensional pressure–temperature (P–T) profiles in radiative–convective and chemical equilibrium. For cloud modeling, we adopt the `EddySed` framework outlined in (A. S. Ackerman & M. S. Marley 2001), a method extensively used in previous studies (A. J. Skemer et al. 2016; C. V. Morley et al. 2015), as well as in model grids such as those from (D. Saumon & M. S. Marley 2008) and the Sonora Diamondback suite (C. V. Morley et al. 2024). Within `PICASO`, we incorporate an updated cloud treatment using `Virga` (N. Batalha et al. 2020), a Python-based implementation of the (A. S. Ackerman & M. S. Marley 2001) model. The mini-grid spans effective temperatures of $T_{\text{eff}} = [275, 300, 325 \text{ K}]$, surface gravity of $\log(g) = 4.25$ (cgs), eddy diffusion parameter of $K_{\text{zz}} = [10^2, 10^7, 10^9 \text{ cm}^2 \text{ s}^{-1}]$, a metallicity of $[M/H] = +0.5$ (relative to the sun), and a solar C/O ratio. Cloudy models have an $f_{\text{sed}} = 8$, with H_2O as the only condensing species. These models are part of a larger grid that will be released in the future, extending the Sonora Bobcat (M. S. Marley et al. 2021a), Sonora Diamondback (C. V. Morley et al. 2024), and Sonora Elf Owl (S. Mukherjee et al. 2024c).

Our custom models differ from the Sonora Elf Owl models in three key aspects of atmospheric chemistry. First, we adopt an updated treatment of CO_2 . Previous studies have shown that Sonora Elf Owl underestimates CO_2 abundances compared to JWST observations of cool substellar objects (S. A. Beiler et al. 2024b). To address this imbalance, we implement a CO_2 kinetic model based on the chemical kinetics described in (K. J. Zahnle & M. S. Marley 2014b),

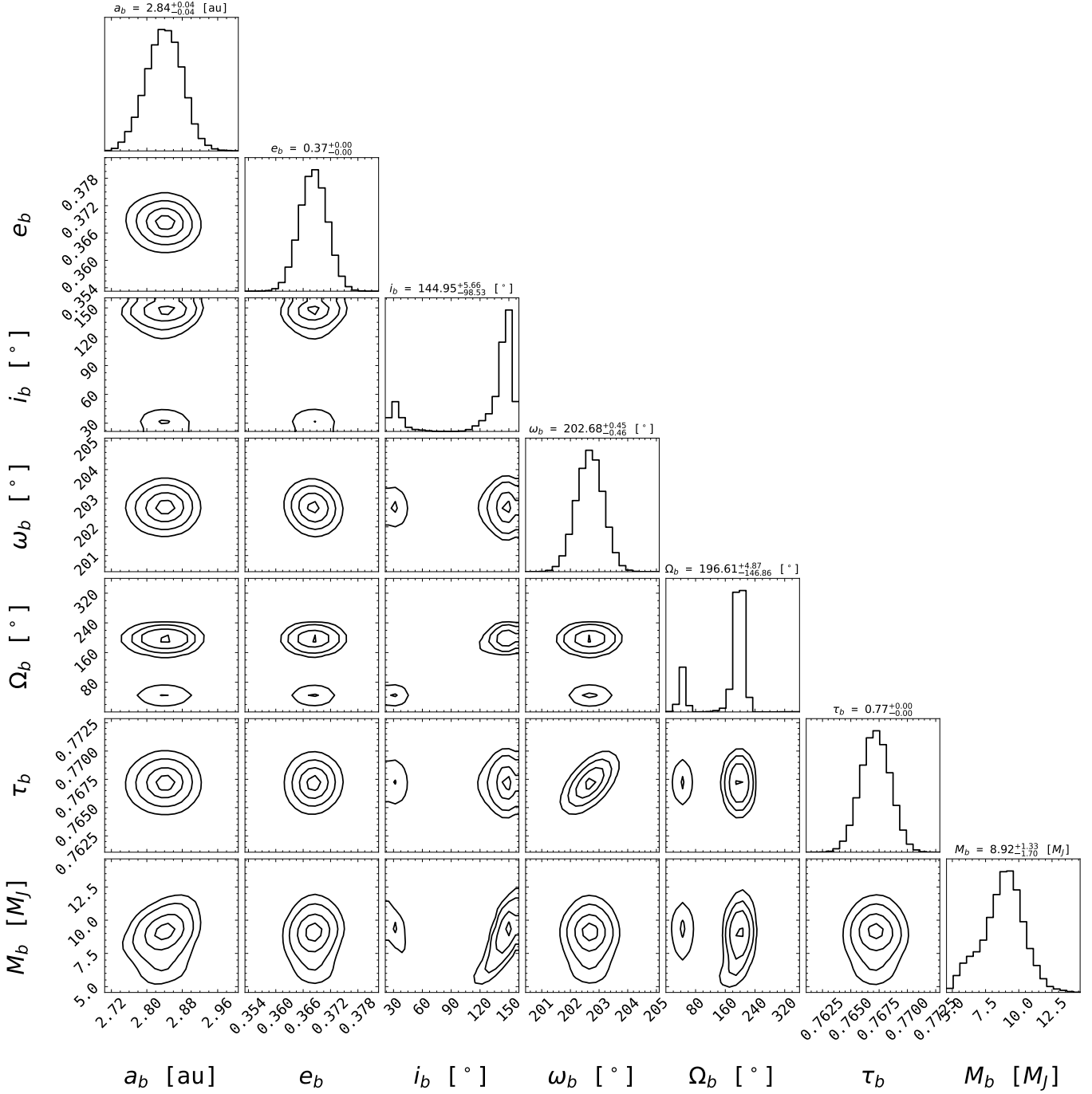


Figure 9. Posterior distribution on the orbital elements of 14 Her b, from the orbitize! orbit fit. Two solutions for the planet’s inclination i_b and longitude of the ascending node Ω_b arise due to the ambiguity of the direction of the planet’s orbit.

507 following recent investigations into its impact (N. F. Wogan et al. 2023; S. Mukherjee et al. 2024a). This update leads
 508 to a stronger CO₂ absorption feature near 4.2 μm . Second, unlike Sonora Elf Owl, our models incorporate rainout
 509 chemistry for condensates such as H₂O, even in cloud-free atmospheres, following the chemical rainout treatment in
 510 the Sonora Bobcat models. Finally, we exclude PH₃, as its abundance was found to be overestimated in Elf Owl
 511 models compared to cool brown dwarf observations (S. A. Beiler et al. 2024b).

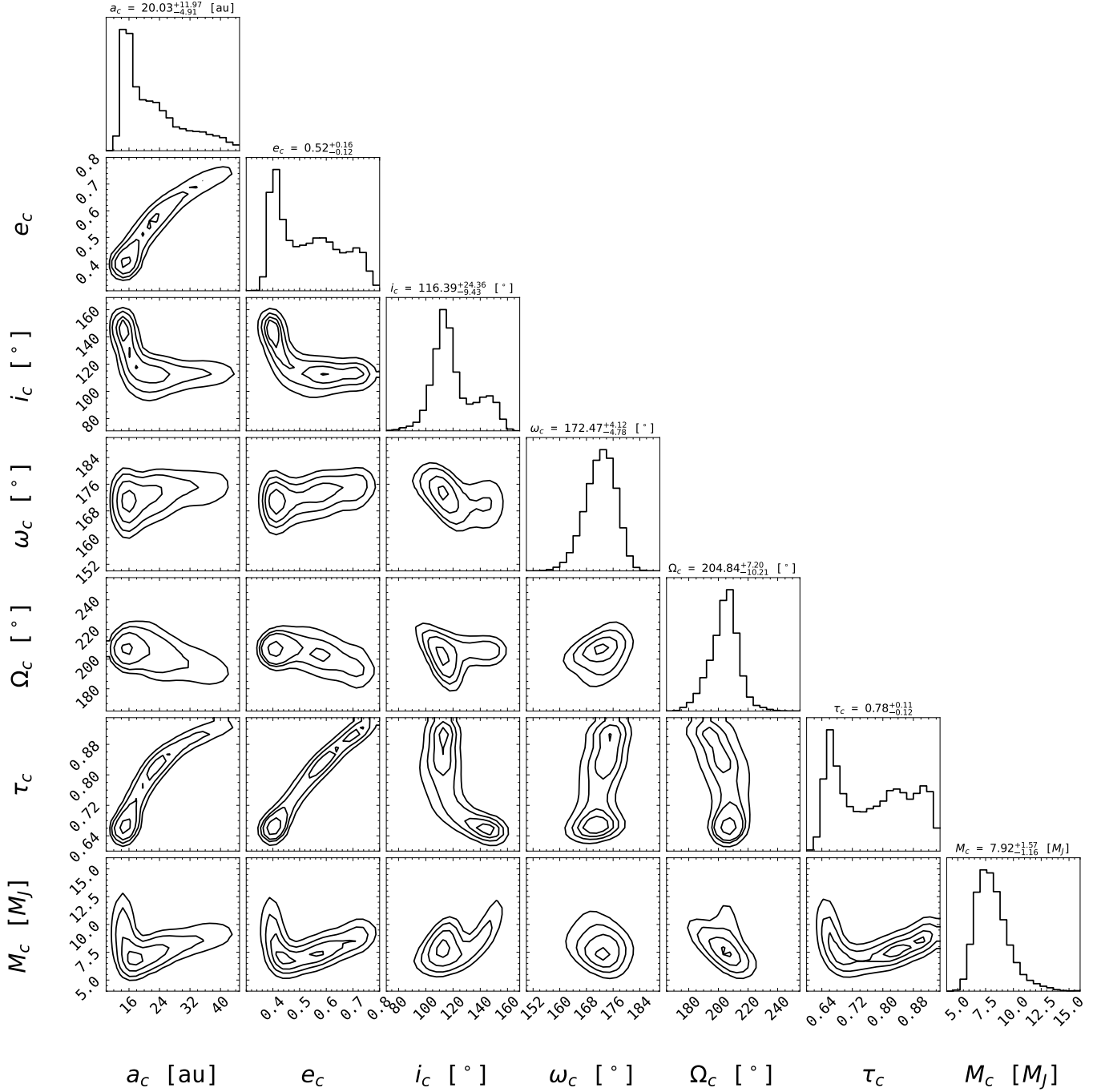


Figure 10. Posterior distribution on the orbital elements of 14 Her c, from the orbitize! orbit fit. Tails on the distributions are correlated with the rv instrumental jitter terms, due to the fractional phase coverage of the observations from various instruments. An additional epoch of JWST/NIRCAM imaging will constrain these parameters dramatically by revising the planet’s eccentricity estimate.

512

D. POTENTIAL FOR VON ZEIPPEL-LIDOV-KOZAI OSCILLATIONS

513 The orbital structure of the 14 Her system suggests the possibility that the system might be experiencing von Zeipel-
 514 Lidov-Kozai (ZLK) oscillations, characterized by coupled high-amplitude eccentricity and inclination oscillations in
 515 misaligned, hierarchical three-body systems between the ZLK critical angles $39.2^\circ < \Theta < 140.8^\circ$. However, the very
 516 concept of ZLK is ill-defined for 14 Her-like systems. The prototypical ZLK effect is defined in the limit of a massless

517 test particle and a massive perturber on a circular orbit. The further a system strays from this regime, the more
 518 the system's secular evolution deviates from traditional ZLK behavior (S. Naoz 2016). In particular, the relatively
 519 equal planetary masses in the 14 Her system make classifying a particular system evolution as ZLK behavior not just
 520 difficult, but arguably meaningless. Regardless of the specific class of oscillation, we emphasize that the system at
 521 present is undoubtedly undergoing extreme mutual dynamical interactions.

522 About 30% of the inferred distribution of the mutual inclination Θ lies between the ZLK critical angles (H. von
 523 Zeipel 1910; M. L. Lidov 1962; Y. Kozai 1962). The ZLK mechanism is thought to have widespread consequences for
 524 planetary systems, including elongating the orbits of comets in our Solar System, as well as triggering high eccentricity
 525 migration of planets to become hot Jupiters (S. Naoz et al. 2011). While a number of extrasolar systems are believed
 526 to have experienced ZLK oscillations in the past (Y. Wu & N. Murray 2003), 14 Her is the first instance in which an
 527 ongoing ZLK mechanism may be observed on a mature system with long-period exoplanets.

REFERENCES

- 528 Ackerman, A. S., & Marley, M. S. 2001, Precipitating
 529 Condensation Clouds in Substellar Atmospheres, *ApJ*,
 530 556, 872, doi: [10.1086/321540](https://doi.org/10.1086/321540)
- 531 Adams Redai, J. I., Follette, K. B., Wang, J., et al. 2023,
 532 The Giant Accreting Protoplanet Survey (GAPlanetS):
 533 Optimization Techniques for Robust Detections of
 534 Protoplanets, *AJ*, 165, 57,
 535 doi: [10.3847/1538-3881/aca60d](https://doi.org/10.3847/1538-3881/aca60d)
- 536 Allard, F., Homeier, D., & Freytag, B. 2011, in
 537 *Astronomical Society of the Pacific Conference Series*,
 538 Vol. 448, 16th Cambridge Workshop on Cool Stars,
 539 Stellar Systems, and the Sun, ed. C. Johns-Krull, M. K.
 540 Browning, & A. A. West, 91,
 541 doi: [10.48550/arXiv.1011.5405](https://doi.org/10.48550/arXiv.1011.5405)
- 542 An, Q., Lu, T., Brandt, G. M., Brandt, T. D., & Li, G.
 543 2025, Significant Mutual Inclinations Between the Stellar
 544 Spin and the Orbits of Both Planets in the HAT-P-11
 545 System, *AJ*, 169, 22, doi: [10.3847/1538-3881/ad90b4](https://doi.org/10.3847/1538-3881/ad90b4)
- 546 Balmer, W. O. 2025, wbalmer/a_herculean_detection: 14
 547 Herculis c JWST coronagraphic imaging, Zenodo,
 548 doi: [10.5281/ZENODO.15483953](https://doi.org/10.5281/ZENODO.15483953)
- 549 Balmer, W. O., Kammerer, J., Pueyo, L., et al. 2025,
 550 JWST-TST High Contrast: Living on the Wedge, or,
 551 NIRCcam Bar Coronagraphy Reveals CO₂ in the HR 8799
 552 and 51 Eri Exoplanets' Atmospheres, *AJ*, 169, 209,
 553 doi: [10.3847/1538-3881/adb1c6](https://doi.org/10.3847/1538-3881/adb1c6)
- 554 Bardalez Gagliuffi, D. C., Faherty, J. K., Li, Y., et al. 2021,
 555 14 Her: A Likely Case of Planet-Planet Scattering, *ApJL*,
 556 922, L43, doi: [10.3847/2041-8213/ac382c](https://doi.org/10.3847/2041-8213/ac382c)
- 557 Batalha, N., caoimherooney11, & sagnickm. 2020,
 558 natashabatalha/virga: Initial Release,, v0.0 Zenodo,
 559 doi: [10.5281/zenodo.3759888](https://doi.org/10.5281/zenodo.3759888)
- 560 Batalha, N. E., Marley, M. S., Lewis, N. K., & Fortney,
 561 J. J. 2019, Exoplanet Reflected-light Spectroscopy with
 562 PICASO, *ApJ*, 878, 70, doi: [10.3847/1538-4357/ab1b51](https://doi.org/10.3847/1538-4357/ab1b51)
- 563 Beiler, S. A., Cushing, M. C., Kirkpatrick, J. D., et al.
 564 2023, The First JWST Spectral Energy Distribution of a
 565 Y Dwarf, *ApJL*, 951, L48, doi: [10.3847/2041-8213/ace32c](https://doi.org/10.3847/2041-8213/ace32c)
- 566 Beiler, S. A., Cushing, M. C., Kirkpatrick, J. D., et al.
 567 2024a, Precise Bolometric Luminosities and Effective
 568 Temperatures of 23 Late-T and Y Dwarfs Obtained with
 569 JWST, *ApJ*, 973, 107, doi: [10.3847/1538-4357/ad6301](https://doi.org/10.3847/1538-4357/ad6301)
- 570 Beiler, S. A., Mukherjee, S., Cushing, M. C., et al. 2024b, A
 571 Tale of Two Molecules: The Underprediction of CO₂ and
 572 Overprediction of PH₃ in Late T and Y Dwarf
 573 Atmospheric Models, *ApJ*, 973, 60,
 574 doi: [10.3847/1538-4357/ad6759](https://doi.org/10.3847/1538-4357/ad6759)
- 575 Benedict, G. F., McArthur, B. E., Nelan, E. P., & Bean,
 576 J. L. 2023, The 14 Her Planetary System: Companion
 577 Masses and Architecture from Radial Velocities and
 578 Astrometry, *AJ*, 166, 27, doi: [10.3847/1538-3881/acd93a](https://doi.org/10.3847/1538-3881/acd93a)
- 579 Blunt, S., Wang, J. J., Angelo, I., et al. 2020, orbitize!/: A
 580 Comprehensive Orbit-fitting Software Package for the
 581 High-contrast Imaging Community, *AJ*, 159, 89,
 582 doi: [10.3847/1538-3881/ab6663](https://doi.org/10.3847/1538-3881/ab6663)
- 583 Bogat, E., Schlieder, J. E., Lawson, K. D., et al. 2025,
 584 Probing the Outskirts of M Dwarf Planetary Systems
 585 with a Cycle 1 JWST NIRCcam Coronagraphy Survey,
 586 arXiv e-prints, arXiv:2504.11659,
 587 doi: [10.48550/arXiv.2504.11659](https://doi.org/10.48550/arXiv.2504.11659)
- 588 Bourrier, V., Lovis, C., Cretignier, M., et al. 2021, The
 589 Rossiter-McLaughlin effect revolutions: an ultra-short
 590 period planet and a warm mini-Neptune on
 591 perpendicular orbits, *A&A*, 654, A152,
 592 doi: [10.1051/0004-6361/202141527](https://doi.org/10.1051/0004-6361/202141527)
- 593 Bowens-Rubin, R., Mang, J., Limbach, M. A., et al. 2025,
 594 NIRCcam yells at cloud: JWST MIRI imaging can
 595 directly detect exoplanets of the same temperature, mass,
 596 age, and orbital separation as Saturn and Jupiter, arXiv
 597 e-prints, arXiv:2505.15995,
 598 doi: [10.48550/arXiv.2505.15995](https://doi.org/10.48550/arXiv.2505.15995)

- 599 Bowler, B. P. 2016, Imaging Extrasolar Giant Planets,
600 PASP, 128, 102001,
601 doi: [10.1088/1538-3873/128/968/102001](https://doi.org/10.1088/1538-3873/128/968/102001)
- 602 Bowler, B. P., Blunt, S. C., & Nielsen, E. L. 2020,
603 Population-level Eccentricity Distributions of Imaged
604 Exoplanets and Brown Dwarf Companions: Dynamical
605 Evidence for Distinct Formation Channels, AJ, 159, 63,
606 doi: [10.3847/1538-3881/ab5b11](https://doi.org/10.3847/1538-3881/ab5b11)
- 607 Brandt, T. D. 2018, The Hipparcos $S = 1$ –2Gaia Catalog of
608 Accelerations, ApJS, 239, 31,
609 doi: [10.3847/1538-4365/aaec06](https://doi.org/10.3847/1538-4365/aaec06)
- 610 Brandt, T. D. 2024a, Optimal Fitting and Debiasing for
611 Detectors Read Out Up-the-Ramp, PASP, 136, 045004,
612 doi: [10.1088/1538-3873/ad38d9](https://doi.org/10.1088/1538-3873/ad38d9)
- 613 Brandt, T. D. 2024b, Likelihood-based Jump Detection and
614 Cosmic Ray Rejection for Detectors Read Out
615 Up-the-ramp, PASP, 136, 045005,
616 doi: [10.1088/1538-3873/ad38da](https://doi.org/10.1088/1538-3873/ad38da)
- 617 Brandt, T. D., Dupuy, T. J., Li, Y., et al. 2021, orvara: An
618 Efficient Code to Fit Orbits Using Radial Velocity,
619 Absolute, and/or Relative Astrometry, AJ, 162, 186,
620 doi: [10.3847/1538-3881/ac042e](https://doi.org/10.3847/1538-3881/ac042e)
- 621 Buchner, J., Georgakakis, A., Nandra, K., et al. 2014, X-ray
622 spectral modelling of the AGN obscuring region in the
623 CDFS: Bayesian model selection and catalogue, A&A,
624 564, A125, doi: [10.1051/0004-6361/201322971](https://doi.org/10.1051/0004-6361/201322971)
- 625 Bushouse, H., Eisenhamer, J., Dencheva, N., et al. 2023,
626 JWST Calibration Pipeline, 1.12.1, Zenodo Zenodo,
627 doi: [10.5281/zenodo.6984365](https://doi.org/10.5281/zenodo.6984365)
- 628 Carson, J. C., Hiner, K. D., Villar, Gregorio G., I., et al.
629 2009, A Distance-Limited Imaging Survey of Substellar
630 Companions to Solar Neighborhood Stars, AJ, 137, 218,
631 doi: [10.1088/0004-6256/137/1/218](https://doi.org/10.1088/0004-6256/137/1/218)
- 632 Carter, A. L., Hinkley, S., Kammerer, J., et al. 2023, The
633 JWST Early Release Science Program for Direct
634 Observations of Exoplanetary Systems I: High-contrast
635 Imaging of the Exoplanet HIP 65426 b from 2 to 16 μm ,
636 ApJL, 951, L20, doi: [10.3847/2041-8213/acd93e](https://doi.org/10.3847/2041-8213/acd93e)
- 637 Czekala, I., Chiang, E., Andrews, S. M., et al. 2019, The
638 Degree of Alignment between Circumbinary Disks and
639 Their Binary Hosts, ApJ, 883, 22,
640 doi: [10.3847/1538-4357/ab287b](https://doi.org/10.3847/1538-4357/ab287b)
- 641 De Rosa, R. J., Dawson, R., & Nielsen, E. L. 2020, A
642 significant mutual inclination between the planets within
643 the π Mensae system, A&A, 640, A73,
644 doi: [10.1051/0004-6361/202038496](https://doi.org/10.1051/0004-6361/202038496)
- 645 Deitrick, R., Barnes, R., McArthur, B., et al. 2015, The
646 Three-dimensional Architecture of the ν Andromedae
647 Planetary System, ApJ, 798, 46,
648 doi: [10.1088/0004-637X/798/1/46](https://doi.org/10.1088/0004-637X/798/1/46)
- 649 Durkan, S., Janson, M., & Carson, J. C. 2016, High
650 Contrast Imaging with Spitzer: Constraining the
651 Frequency of Giant Planets out to 1000 au Separations,
652 ApJ, 824, 58, doi: [10.3847/0004-637X/824/1/58](https://doi.org/10.3847/0004-637X/824/1/58)
- 653 Eggleton, P. P., & Kiseleva-Eggleton, L. 2001, Orbital
654 Evolution in Binary and Triple Stars, with an Application
655 to SS Lacertae, ApJ, 562, 1012, doi: [10.1086/323843](https://doi.org/10.1086/323843)
- 656 Eisenstein, D. J., Johnson, B. D., Robertson, B., et al.
657 2023, The JADES Origins Field: A New JWST Deep
658 Field in the JADES Second NIRCcam Data Release,
659 arXiv e-prints, arXiv:2310.12340,
660 doi: [10.48550/arXiv.2310.12340](https://doi.org/10.48550/arXiv.2310.12340)
- 661 Fabrycky, D., & Tremaine, S. 2007, Shrinking Binary and
662 Planetary Orbits by Kozai Cycles with Tidal Friction,
663 ApJ, 669, 1298, doi: [10.1086/521702](https://doi.org/10.1086/521702)
- 664 Feng, F., Xiao, G.-Y., Jones, H. R. A., et al. 2024, Lessons
665 learned from the detection of wide companions by radial
666 velocity and astrometry, arXiv e-prints,
667 arXiv:2412.14542, doi: [10.48550/arXiv.2412.14542](https://doi.org/10.48550/arXiv.2412.14542)
- 668 Feng, F., Butler, R. P., Vogt, S. S., et al. 2022, 3D Selection
669 of 167 Substellar Companions to Nearby Stars, ApJS,
670 262, 21, doi: [10.3847/1538-4365/ac7e57](https://doi.org/10.3847/1538-4365/ac7e57)
- 671 Feroz, F., Hobson, M. P., & Bridges, M. 2009,
672 MULTINEST: an efficient and robust Bayesian inference
673 tool for cosmology and particle physics, MNRAS, 398,
674 1601, doi: [10.1111/j.1365-2966.2009.14548.x](https://doi.org/10.1111/j.1365-2966.2009.14548.x)
- 675 Follette, K. B. 2023, An Introduction to High Contrast
676 Differential Imaging of Exoplanets and Disks, PASP, 135,
677 093001, doi: [10.1088/1538-3873/aceb31](https://doi.org/10.1088/1538-3873/aceb31)
- 678 Foreman-Mackey, D., Hogg, D. W., Lang, D., & Goodman,
679 J. 2013, emcee: The MCMC Hammer, PASP, 125, 306,
680 doi: [10.1086/670067](https://doi.org/10.1086/670067)
- 681 Franson, K., Balmer, W. O., Bowler, B. P., et al. 2024a,
682 JWST/NIRCam 4–5 μm Imaging of the Giant Planet AF
683 Lep b, ApJL, 974, L11, doi: [10.3847/2041-8213/ad736a](https://doi.org/10.3847/2041-8213/ad736a)
- 684 Franson, K., Balmer, W. O., Bowler, B. P., et al. 2024b,
685 JWST/NIRCam 4–5 μm Imaging of the Giant Planet AF
686 Lep b, ApJL, 974, L11, doi: [10.3847/2041-8213/ad736a](https://doi.org/10.3847/2041-8213/ad736a)
- 687 Gaia Collaboration, Brown, A. G. A., Vallenari, A., et al.
688 2021, Gaia Early Data Release 3. Summary of the
689 contents and survey properties, A&A, 649, A1,
690 doi: [10.1051/0004-6361/202039657](https://doi.org/10.1051/0004-6361/202039657)
- 691 Gaia Collaboration, Vallenari, A., Brown, A. G. A., et al.
692 2022, Gaia Data Release 3: Summary of the content and
693 survey properties, arXiv e-prints, arXiv:2208.00211,
694 doi: [10.48550/arXiv.2208.00211](https://doi.org/10.48550/arXiv.2208.00211)

- 695 Girard, J. H., Gennaro, M., Rest, A., et al. 2024, in Space
696 Telescopes and Instrumentation 2024: Optical, Infrared,
697 and Millimeter Wave, ed. L. E. Coyle, S. Matsuura, &
698 M. D. Perrin, Vol. 13092, International Society for Optics
699 and Photonics (SPIE), 1309251, doi: [10.1117/12.3020243](https://doi.org/10.1117/12.3020243)
- 700 Golomb, J., Rocha, G., Meshkat, T., et al. 2021,
701 PlanetEvidence: Planet or Noise?, AJ, 162, 304,
702 doi: [10.3847/1538-3881/ac174e](https://doi.org/10.3847/1538-3881/ac174e)
- 703 Gonzalez, G., Wallerstein, G., & Saar, S. H. 1999, Parent
704 Stars of Extrasolar Planets. IV. 14 Herculis, HD 187123,
705 and HD 210277, ApJL, 511, L111, doi: [10.1086/311847](https://doi.org/10.1086/311847)
- 706 Groff, T. D., Zimmerman, N. T., Subedi, H. B., et al. 2021,
707 in Society of Photo-Optical Instrumentation Engineers
708 (SPIE) Conference Series, Vol. 11443, Society of
709 Photo-Optical Instrumentation Engineers (SPIE)
710 Conference Series, ed. M. Lystrup & M. D. Perrin,
711 114433D, doi: [10.1117/12.2562925](https://doi.org/10.1117/12.2562925)
- 712 Hanel, R., Conrath, B., Herath, L., Kunde, V., & Pirraglia,
713 J. 1981, Albedo, internal heat, and energy balance of
714 Jupiter - Preliminary results of the Voyager infrared
715 investigation, J. Geophys. Res., 86, 8705,
716 doi: [10.1029/JA086iA10p08705](https://doi.org/10.1029/JA086iA10p08705)
- 717 Hinkley, S., Lacour, S., Marleau, G. D., et al. 2023, Direct
718 discovery of the inner exoplanet in the HD 206893
719 system. Evidence for deuterium burning in a
720 planetary-mass companion, A&A, 671, L5,
721 doi: [10.1051/0004-6361/202244727](https://doi.org/10.1051/0004-6361/202244727)
- 722 Høg, E., Fabricius, C., Makarov, V. V., et al. 2000, The
723 Tycho-2 catalogue of the 2.5 million brightest stars,
724 A&A, 355, L27
- 725 Kammerer, J., Girard, J., Carter, A. L., et al. 2022, in
726 Society of Photo-Optical Instrumentation Engineers
727 (SPIE) Conference Series, Vol. 12180, Space Telescopes
728 and Instrumentation 2022: Optical, Infrared, and
729 Millimeter Wave, ed. L. E. Coyle, S. Matsuura, & M. D.
730 Perrin, 121803N, doi: [10.1117/12.2628865](https://doi.org/10.1117/12.2628865)
- 731 Kammerer, J., Lawson, K., Perrin, M. D., et al. 2024,
732 JWST-TST High Contrast: JWST/NIRCam observations
733 of the young giant planet β Pic b, arXiv e-prints,
734 arXiv:2405.18422, doi: [10.48550/arXiv.2405.18422](https://doi.org/10.48550/arXiv.2405.18422)
- 735 Kirkpatrick, J. D., Marocco, F., Gelino, C. R., et al. 2024,
736 The Initial Mass Function Based on the Full-sky 20 pc
737 Census of \sim 3600 Stars and Brown Dwarfs, ApJS, 271,
738 55, doi: [10.3847/1538-4365/ad24e2](https://doi.org/10.3847/1538-4365/ad24e2)
- 739 Kozai, Y. 1962, Secular Perturbations of Asteroids with
740 High Inclination and Eccentricity., AJ, 67, 579,
741 doi: [10.1086/108876](https://doi.org/10.1086/108876)
- 742 Krist, J. E., Balasubramanian, K., Muller, R. E., et al.
743 2010, in Society of Photo-Optical Instrumentation
744 Engineers (SPIE) Conference Series, Vol. 7731, Space
745 Telescopes and Instrumentation 2010: Optical, Infrared,
746 and Millimeter Wave, ed. J. Oschmann, Jacobus M.,
747 M. C. Clampin, & H. A. MacEwen, 77313J,
748 doi: [10.1117/12.856488](https://doi.org/10.1117/12.856488)
- 749 Lacour, S., Wang, J. J., Rodet, L., et al. 2021, The mass of
750 β Pictoris c from β Pictoris b orbital motion, A&A, 654,
751 L2, doi: [10.1051/0004-6361/202141889](https://doi.org/10.1051/0004-6361/202141889)
- 752 Lacy, B., & Burrows, A. 2023, Self-consistent Models of Y
753 Dwarf Atmospheres with Water Clouds and
754 Disequilibrium Chemistry, ApJ, 950, 8,
755 doi: [10.3847/1538-4357/acc8cb](https://doi.org/10.3847/1538-4357/acc8cb)
- 756 Lagrange, A. M., Bonnefoy, M., Chauvin, G., et al. 2010, A
757 Giant Planet Imaged in the Disk of the Young Star β
758 Pictoris, Science, 329, 57, doi: [10.1126/science.1187187](https://doi.org/10.1126/science.1187187)
- 759 Lagrange, A. M., Wilkinson, C., Mâlin, M., et al. 2025a,
760 Evidence for a sub-jovian planet in the young TWA7
761 disk, arXiv e-prints, arXiv:2502.15081,
762 doi: [10.48550/arXiv.2502.15081](https://doi.org/10.48550/arXiv.2502.15081)
- 763 Lagrange, A. M., Wilkinson, C., Mâlin, M., et al. 2025b,
764 Evidence for a sub-jovian planet in the young TWA7
765 disk, arXiv e-prints, arXiv:2502.15081,
766 doi: [10.48550/arXiv.2502.15081](https://doi.org/10.48550/arXiv.2502.15081)
- 767 Leisenring, J., Schlawin, E., & Fraine, J. 2022,
768 JarronL/pynrc: Release v1.0.4., v1.0.4, Zenodo Zenodo,
769 doi: [10.5281/zenodo.5829553](https://doi.org/10.5281/zenodo.5829553)
- 770 Lidov, M. L. 1962, The evolution of orbits of artificial
771 satellites of planets under the action of gravitational
772 perturbations of external bodies, Planet. Space Sci., 9,
773 719, doi: [10.1016/0032-0633\(62\)90129-0](https://doi.org/10.1016/0032-0633(62)90129-0)
- 774 Lindegren, L. 2018, Re-Normalising the Astrometric
775 Chi-Square in Gaia DR2., Tech. Rep.
776 GAIA-C3-TN-LU-LL-124-01
- 777 Lu, T., An, Q., Li, G., et al. 2025, Planet-Planet Scattering
778 and Von Zeipel-Lidov-Kozai Migration—The Dynamical
779 History of HAT-P-11, ApJ, 979, 218,
780 doi: [10.3847/1538-4357/ad9b79](https://doi.org/10.3847/1538-4357/ad9b79)
- 781 Luck, R. E., & Heiter, U. 2006, Dwarfs in the Local Region,
782 AJ, 131, 3069, doi: [10.1086/504080](https://doi.org/10.1086/504080)
- 783 Luhman, K. L., & Jayawardhana, R. 2002, An Adaptive
784 Optics Search for Companions to Stars with Planets,
785 ApJ, 566, 1132, doi: [10.1086/338338](https://doi.org/10.1086/338338)
- 786 Mandt, K. E., Lustig-Yaeger, J., Luspay-Kuti, A., et al.
787 2024, A nearly terrestrial D/H for comet
788 67P/Churyumov-Gerasimenko, Science Advances, 10,
789 eadp2191, doi: [10.1126/sciadv.adp2191](https://doi.org/10.1126/sciadv.adp2191)

- 790 Marley, M. S., Saumon, D., Visscher, C., et al. 2021a, The
791 Sonora Brown Dwarf Atmosphere and Evolution Models.
792 I. Model Description and Application to Cloudless
793 Atmospheres in Rainout Chemical Equilibrium, *ApJ*,
794 920, 85, doi: [10.3847/1538-4357/ac141d](https://doi.org/10.3847/1538-4357/ac141d)
- 795 Marley, M. S., Saumon, D., Visscher, C., et al. 2021b, The
796 Sonora Brown Dwarf Atmosphere and Evolution Models.
797 I. Model Description and Application to Cloudless
798 Atmospheres in Rainout Chemical Equilibrium, *ApJ*,
799 920, 85, doi: [10.3847/1538-4357/ac141d](https://doi.org/10.3847/1538-4357/ac141d)
- 800 Marois, C., Macintosh, B., Barman, T., et al. 2008, *Direct*
801 *Imaging of Multiple Planets Orbiting the Star HR 8799*,
802 *Science*, 322, 1348, doi: [10.1126/science.1166585](https://doi.org/10.1126/science.1166585)
- 803 Matthews, E. C., Carter, A. L., Pathak, P., et al. 2024a, A
804 temperate super-Jupiter imaged with JWST in the
805 mid-infrared, *Nature*, 633, 789,
806 doi: [10.1038/s41586-024-07837-8](https://doi.org/10.1038/s41586-024-07837-8)
- 807 Matthews, E. C., Carter, A. L., Pathak, P., et al. 2024b, A
808 temperate super-Jupiter imaged with JWST in the
809 mid-infrared, *Nature*, 633, 789,
810 doi: [10.1038/s41586-024-07837-8](https://doi.org/10.1038/s41586-024-07837-8)
- 811 Mawet, D., Milli, J., Wahhaj, Z., et al. 2014, *Fundamental*
812 *Limitations of High Contrast Imaging Set by Small*
813 *Sample Statistics*, *ApJ*, 792, 97,
814 doi: [10.1088/0004-637X/792/2/97](https://doi.org/10.1088/0004-637X/792/2/97)
- 815 McArthur, B. E., Benedict, G. F., Barnes, R., et al. 2010,
816 *New Observational Constraints on the ν Andromedae*
817 *System with Data from the Hubble Space Telescope and*
818 *Hobby-Eberly Telescope*, *ApJ*, 715, 1203,
819 doi: [10.1088/0004-637X/715/2/1203](https://doi.org/10.1088/0004-637X/715/2/1203)
- 820 Merlin, E., Santini, P., Paris, D., et al. 2024,
821 *ASTRODEEP-JWST: NIRCam-HST multi-band*
822 *photometry and redshifts for half a million sources in six*
823 *extragalactic deep fields*, *A&A*, 691, A240,
824 doi: [10.1051/0004-6361/202451409](https://doi.org/10.1051/0004-6361/202451409)
- 825 Miles, B. E., Skemer, A. J. I., Morley, C. V., et al. 2020,
826 *Observations of Disequilibrium CO Chemistry in the*
827 *Coldest Brown Dwarfs*, *AJ*, 160, 63,
828 doi: [10.3847/1538-3881/ab9114](https://doi.org/10.3847/1538-3881/ab9114)
- 829 Mills, S. M., & Fabrycky, D. C. 2017, *Kepler-108: A*
830 *Mutually Inclined Giant Planet System*, *AJ*, 153, 45,
831 doi: [10.3847/1538-3881/153/1/45](https://doi.org/10.3847/1538-3881/153/1/45)
- 832 Morley, C. V., Fortney, J. J., Marley, M. S., et al. 2015,
833 *Thermal Emission and Reflected Light Spectra of Super*
834 *Earths with Flat Transmission Spectra*, *ApJ*, 815, 110,
835 doi: [10.1088/0004-637X/815/2/110](https://doi.org/10.1088/0004-637X/815/2/110)
- 836 Morley, C. V., Mukherjee, S., Marley, M. S., et al. 2024,
837 *The Sonora Substellar Atmosphere Models. III.*
838 *Diamondback: Atmospheric Properties, Spectra, and*
839 *Evolution for Warm Cloudy Substellar Objects*, arXiv
840 e-prints, arXiv:2402.00758,
841 doi: [10.48550/arXiv.2402.00758](https://doi.org/10.48550/arXiv.2402.00758)
- 842 Mukherjee, S., Batalha, N. E., Fortney, J. J., & Marley,
843 M. S. 2023, *PICASO 3.0: A One-dimensional Climate*
844 *Model for Giant Planets and Brown Dwarfs*, *ApJ*, 942,
845 71, doi: [10.3847/1538-4357/ac9f48](https://doi.org/10.3847/1538-4357/ac9f48)
- 846 Mukherjee, S., Fortney, J. J., Wogan, N. F., Sing, D. K., &
847 Ohno, K. 2024a, *Effects of Planetary Parameters on*
848 *Disequilibrium Chemistry in Irradiated Planetary*
849 *Atmospheres: From Gas Giants to Sub-Neptunes*, arXiv
850 e-prints, arXiv:2410.17169,
851 doi: [10.48550/arXiv.2410.17169](https://doi.org/10.48550/arXiv.2410.17169)
- 852 Mukherjee, S., Fortney, J. J., Morley, C. V., et al. 2024b,
853 *The Sonora Substellar Atmosphere Models. IV. Elf Owl:*
854 *Atmospheric Mixing and Chemical Disequilibrium with*
855 *Varying Metallicity and C/O Ratios*, *ApJ*, 963, 73,
856 doi: [10.3847/1538-4357/ad18c2](https://doi.org/10.3847/1538-4357/ad18c2)
- 857 Mukherjee, S., Fortney, J. J., Morley, C. V., et al. 2024c,
858 *The Sonora Substellar Atmosphere Models. IV. Elf Owl:*
859 *Atmospheric Mixing and Chemical Disequilibrium with*
860 *Varying Metallicity and C/O Ratios*, *ApJ*, 963, 73,
861 doi: [10.3847/1538-4357/ad18c2](https://doi.org/10.3847/1538-4357/ad18c2)
- 862 Naef, D., Mayor, M., Beuzit, J. L., et al. 2004, *The*
863 *ELODIE survey for northern extra-solar planets. III.*
864 *Three planetary candidates detected with ELODIE*,
865 *A&A*, 414, 351, doi: [10.1051/0004-6361:20034091](https://doi.org/10.1051/0004-6361:20034091)
- 866 Naoz, S. 2016, *The Eccentric Kozai-Lidov Effect and Its*
867 *Applications*, *ARA&A*, 54, 441,
868 doi: [10.1146/annurev-astro-081915-023315](https://doi.org/10.1146/annurev-astro-081915-023315)
- 869 Naoz, S., Farr, W. M., Lithwick, Y., Rasio, F. A., &
870 Teyssandier, J. 2011, *Hot Jupiters from secular*
871 *planet-planet interactions*, *Nature*, 473, 187,
872 doi: [10.1038/nature10076](https://doi.org/10.1038/nature10076)
- 873 Naoz, S., Farr, W. M., Lithwick, Y., Rasio, F. A., &
874 Teyssandier, J. 2013, *Secular dynamics in hierarchical*
875 *three-body systems*, *MNRAS*, 431, 2155,
876 doi: [10.1093/mnras/stt302](https://doi.org/10.1093/mnras/stt302)
- 877 Nesvorný, D. 2011, *Young Solar System's Fifth Giant*
878 *Planet?*, *ApJL*, 742, L22,
879 doi: [10.1088/2041-8205/742/2/L22](https://doi.org/10.1088/2041-8205/742/2/L22)
- 880 Patience, J., White, R. J., Ghez, A. M., et al. 2002, *Stellar*
881 *Companions to Stars with Planets*, *ApJ*, 581, 654,
882 doi: [10.1086/342982](https://doi.org/10.1086/342982)

- 883 Pueyo, L. 2016, Detection and Characterization of
884 Exoplanets using Projections on Karhunen Loeve
885 Eigenimages: Forward Modeling, *ApJ*, 824, 117,
886 doi: [10.3847/0004-637X/824/2/117](https://doi.org/10.3847/0004-637X/824/2/117)
- 887 Raymond, S. N. 2024, The Solar System: structural
888 overview, origins and evolution, arXiv e-prints,
889 arXiv:2404.14982, doi: [10.48550/arXiv.2404.14982](https://doi.org/10.48550/arXiv.2404.14982)
- 890 Rieke, M. J., Robertson, B., Tacchella, S., et al. 2023,
891 JADES Initial Data Release for the Hubble Ultra Deep
892 Field: Revealing the Faint Infrared Sky with Deep JWST
893 NIRCcam Imaging, *ApJS*, 269, 16,
894 doi: [10.3847/1538-4365/acf44d](https://doi.org/10.3847/1538-4365/acf44d)
- 895 Rigby, J., Perrin, M., McElwain, M., et al. 2023, The
896 Science Performance of JWST as Characterized in
897 Commissioning, *PASP*, 135, 048001,
898 doi: [10.1088/1538-3873/acb293](https://doi.org/10.1088/1538-3873/acb293)
- 899 Rodigas, T. J., Males, J. R., Hinz, P. M., Mamajek, E. E.,
900 & Knox, R. P. 2011, Direct Imaging Constraints on the
901 Putative Exoplanet 14 Her C, *ApJ*, 732, 10,
902 doi: [10.1088/0004-637X/732/1/10](https://doi.org/10.1088/0004-637X/732/1/10)
- 903 Rosenthal, L. J., Fulton, B. J., Hirsch, L. A., et al. 2021,
904 The California Legacy Survey. I. A Catalog of 178
905 Planets from Precision Radial Velocity Monitoring of 719
906 Nearby Stars over Three Decades, *ApJS*, 255, 8,
907 doi: [10.3847/1538-4365/abe23c](https://doi.org/10.3847/1538-4365/abe23c)
- 908 Rowland, M. J., Morley, C. V., Miles, B. E., et al. 2024,
909 Protosolar D-to-H Abundance and One Part per Billion
910 PH₃ in the Coldest Brown Dwarf, *ApJL*, 977, L49,
911 doi: [10.3847/2041-8213/ad9744](https://doi.org/10.3847/2041-8213/ad9744)
- 912 Saumon, D., & Marley, M. S. 2008, The Evolution of L and
913 T Dwarfs in Color-Magnitude Diagrams, *ApJ*, 689, 1327,
914 doi: [10.1086/592734](https://doi.org/10.1086/592734)
- 915 Skemer, A. J., Morley, C. V., Allers, K. N., et al. 2016, The
916 First Spectrum of the Coldest Brown Dwarf, *ApJL*, 826,
917 L17, doi: [10.3847/2041-8205/826/2/L17](https://doi.org/10.3847/2041-8205/826/2/L17)
- 918 Skrutskie, M. F., Cutri, R. M., Stiening, R., et al. 2006,
919 The Two Micron All Sky Survey (2MASS), *AJ*, 131,
920 1163, doi: [10.1086/498708](https://doi.org/10.1086/498708)
- 921 Soubiran, C., Le Campion, J. F., Cayrel de Strobel, G., &
922 Caillo, A. 2010, The PASTEL catalogue of stellar
923 parameters, *A&A*, 515, A111,
924 doi: [10.1051/0004-6361/201014247](https://doi.org/10.1051/0004-6361/201014247)
- 925 Soummer, R., Lajoie, C.-P., Pueyo, L., et al. 2014, in
926 Society of Photo-Optical Instrumentation Engineers
927 (SPIE) Conference Series, Vol. 9143, Space Telescopes
928 and Instrumentation 2014: Optical, Infrared, and
929 Millimeter Wave, ed. J. Oschmann, Jacobus M.,
930 M. Clampin, G. G. Fazio, & H. A. MacEwen, 91433V,
931 doi: [10.1117/12.2057190](https://doi.org/10.1117/12.2057190)
- 932 Soummer, R., Pueyo, L., & Larkin, J. 2012, Detection and
933 Characterization of Exoplanets and Disks Using
934 Projections on Karhunen-Loève Eigenimages, *ApJL*, 755,
935 L28, doi: [10.1088/2041-8205/755/2/L28](https://doi.org/10.1088/2041-8205/755/2/L28)
- 936 Sumi, T., Koshimoto, N., Bennett, D. P., et al. 2023,
937 Free-floating Planet Mass Function from MOA-II 9 yr
938 Survey toward the Galactic Bulge, *AJ*, 166, 108,
939 doi: [10.3847/1538-3881/ace688](https://doi.org/10.3847/1538-3881/ace688)
- 940 Teyssandier, J., Naoz, S., Lizarraga, I., & Rasio, F. A.
941 2013, Extreme Orbital Evolution from Hierarchical
942 Secular Coupling of Two Giant Planets, *ApJ*, 779, 166,
943 doi: [10.1088/0004-637X/779/2/166](https://doi.org/10.1088/0004-637X/779/2/166)
- 944 Vogt, S. S., Radovan, M., Kibrick, R., et al. 2014,
945 APF—The Lick Observatory Automated Planet Finder,
946 *PASP*, 126, 359, doi: [10.1086/676120](https://doi.org/10.1086/676120)
- 947 von Zeipel, H. 1910, Sur l'application des séries de M.
948 Lindstedt à l'étude du mouvement des comètes
949 périodiques, *Astronomische Nachrichten*, 183, 345,
950 doi: [10.1002/asna.19091832202](https://doi.org/10.1002/asna.19091832202)
- 951 Vousden, W., Farr, W. M., & Mandel, I. 2021, ptemcee: A
952 parallel-tempered version of emcee,
953 <http://ascl.net/2101.006>
- 954 Wang, J. J., Ruffio, J.-B., De Rosa, R. J., et al. 2015,
955 pyKLIP: PSF Subtraction for Exoplanets and Disks,,
956 Astrophysics Source Code Library, record ascl:1506.001
957 <http://ascl.net/1506.001>
- 958 Wang, J. J., Graham, J. R., Pueyo, L., et al. 2016, The
959 Orbit and Transit Prospects for β Pictoris b Constrained
960 with One Milliarcsecond Astrometry, *AJ*, 152, 97,
961 doi: [10.3847/0004-6256/152/4/97](https://doi.org/10.3847/0004-6256/152/4/97)
- 962 Wang, J. J., Graham, J. R., Dawson, R., et al. 2018,
963 Dynamical Constraints on the HR 8799 Planets with
964 GPI, *AJ*, 156, 192, doi: [10.3847/1538-3881/aae150](https://doi.org/10.3847/1538-3881/aae150)
- 965 Wittenmyer, R. A., Endl, M., & Cochran, W. D. 2007,
966 Long-Period Objects in the Extrasolar Planetary
967 Systems 47 Ursae Majoris and 14 Herculis, *ApJ*, 654,
968 625, doi: [10.1086/509110](https://doi.org/10.1086/509110)
- 969 Wogan, N. F., Catling, D. C., Zahnle, K. J., & Lupu, R.
970 2023, Origin-of-life Molecules in the Atmosphere after
971 Big Impacts on the Early Earth, *PSJ*, 4, 169,
972 doi: [10.3847/PSJ/aced83](https://doi.org/10.3847/PSJ/aced83)
- 973 Wu, Y., & Murray, N. 2003, Planet Migration and Binary
974 Companions: The Case of HD 80606b, *ApJ*, 589, 605,
975 doi: [10.1086/374598](https://doi.org/10.1086/374598)
- 976 Xuan, J. W., & Wyatt, M. C. 2020, Evidence for a high
977 mutual inclination between the cold Jupiter and
978 transiting super Earth orbiting π Men, *MNRAS*, 497,
979 2096, doi: [10.1093/mnras/staa2033](https://doi.org/10.1093/mnras/staa2033)

980 Zahnle, K. J., & Marley, M. S. 2014a, Methane, Carbon
981 Monoxide, and Ammonia in Brown Dwarfs and
982 Self-Luminous Giant Planets, ApJ, 797, 41,
983 doi: [10.1088/0004-637X/797/1/41](https://doi.org/10.1088/0004-637X/797/1/41)

984 Zahnle, K. J., & Marley, M. S. 2014b, Methane, Carbon
985 Monoxide, and Ammonia in Brown Dwarfs and
986 Self-Luminous Giant Planets, ApJ, 797, 41,
987 doi: [10.1088/0004-637X/797/1/41](https://doi.org/10.1088/0004-637X/797/1/41)
988 Zhang, J., Weiss, L. M., Huber, D., et al. 2024, Discovery of
989 a Jupiter Analog Misaligned to the Inner Planetary
990 System in HD 73344, arXiv e-prints, arXiv:2408.09614,
991 doi: [10.48550/arXiv.2408.09614](https://doi.org/10.48550/arXiv.2408.09614)